The magmatic and eruptive evolution of the 1883 caldera-forming eruption of Krakatau

Madden-nadeau, A.l.; Cassidy, M.; Pyle, D.m.; Mather, T.A.; Watt, Sebastian; Engwell, S.l.; Abdurrachman, M.; Nurshal, M.e.m.; Tappin, D.r.; Ismail, T.

DOI:
10.1016/j.jvolgeores.2021.107176

The magmatic and eruptive evolution of the 1883 caldera-forming eruption of Krakatau: integrating field- to crystal-scale observations

Madden-Nadeau, A.L.[1*], Cassidy, M.[1], Pyle, D.M.[1], Mather, T.A.[1], Watt, S.F.L.[2], Engwell, S.L.[3], Abdurrachman, M.[4], Nurshal, M.E.M.[4], Tappin, D.R.[5,6] & Ismail, T.[7]

amber.madden-nadeau@univ.ox.ac.uk

[1]Department of Earth Sciences, University of Oxford, South Parks Road, Oxford OX1 3AN UK

[2]School of Geography, Earth and Environmental Sciences, University of Birmingham, Edgbaston, Birmingham B15 2TT UK

[3]British Geological Survey, The Lyell Centre, Research Avenue South, Edinburgh, EH14 4AP UK

[4]Faculty of Earth Sciences and Technology, Institut Teknologi Bandung, Jalan Ganesa No. 10 Bandung 40132, West Java, Indonesia

[5]British Geological Survey, Nicker Hill, Keyworth, Nottingham NG12 5GG, UK

[6]Dept. of Earth Sciences, University College, London, WC1E 6BT, UK

[7]Department of Geology, Sekolah Tinggi Teknologi Mineral Indonesia, Bandung 40263, West Java, Indonesia

Abstract

Explosive, caldera-forming eruptions are exceptional and hazardous volcanic phenomena. The 1883 eruption of Krakatau is the largest such event for which there are detailed contemporary written accounts, allowing information on the eruptive progression to be integrated with the stratigraphy and geochemistry of its products. Freshly exposed sequences of the 1883 eruptive deposits of Krakatau, stripped of vegetation by a tsunami generated by the flank collapse of Anak Krakatau in 2018, shed new light on the eruptive sequence. Matrix glass from the base of the stratigraphy is chemically distinct and more evolved than the overlying sequence indicating the presence of a shallow, silicic melt-rich region that was evacuated during the early eruptive activity from May 1883 onwards. Disruption of the shallow, silicic magma may have led to the coalescence and mixing of chemically similar melts representative of a range of magmatic conditions, as evidenced by complex and varied plagioclase phenocryst zoning profiles. This mixing, over a period of two to three months, culminated in the onset of the climactic phase of the eruption on 26th August 1883. Pyroclastic density currents (PDCs) emplaced during this phase of the eruption show a change in transport direction from north east to south west, coinciding with the deposition of a lithic lag breccia unit. This may be attributed to partial collapse of an elevated portion of the island, resulting in the removal of a topographic barrier. Edifice destruction potentially further reduced the overburden on the underlying magmatic system, leading to the most explosive and energetic phase of the eruption in the morning of 27th August 1883. This phase of the eruption culminated in a final period of caldera collapse, which is recorded in the stratigraphy as a second lithic lag breccia. The massive PDC deposits emplaced during this final phase contain glassy blocks up to 8 m in size, observed for the first time in 2019, which are chemically similar to the pyroclastic sequence. These blocks are interpreted as representing stagnant, shallow portions of the magma reservoir disrupted during the final stages of caldera formation. This study provides new evidence for the role that precursory eruptions and amalgamation of shallow crustal magma bodies potentially play in the months leading up to caldera-forming eruptions.

Keywords: Caldera, stratigraphy, petrology, geochemistry, fieldwork

1. Introduction

The 1883 eruption of Krakatau (or Krakatoa) is one of the most infamous volcanic disasters, and the first caldera-forming eruption in history to make headline news around the world (Symons et al., 1888). The eruption demonstrated that violent, caldera-forming eruptions can have not only devastating local effects, but also global impacts (Verbeek, 1884; Symons et al., 1888; Simkin and Fiske, 1983). Subsequent work on other caldera-forming systems shows that these high-magnitude, low-frequency events may have very long build-up phases, characterised by both effusive and weakly explosive activity (e.g., Forni et al., 2018; Druitt et al., 2019). Long-term shifts in eruptive style are poorly understood in general, but this is particularly the case for caldera systems, as there has not yet been the opportunity to monitor any volcano during the long run-up through to a caldera-forming eruption; this poses challenges for the interpretation of contemporary geophysical data in volcano monitoring (e.g., Newhall and Dzurisin, 1988; Gottsmann and Marti, 2008; Druitt et al., 2012). Petrological tools offer a unique insight into the architecture of pre-eruptive magma plumbing systems, and the conditions leading up to eruption. The 1883 eruption of Krakatau is particularly useful in this regard, as it is the largest known eruption for which there are multiple documented observations in contemporary accounts, which allow the eruption progression to be integrated with other datasets, analogous to studies of the 79 AD eruption of Vesuvius (e.g. Sigurdsson et al., 1982; Cioni et al., 2000).

Physical and chemical properties of a magma influence its ascent rate and ability to outgas, and are in turn strongly linked with eruptive style (Cassidy et al., 2018). Petrological data allow pre-eruptive magma storage conditions, such as pressure, temperature and volatile content, to be constrained. Pressure is an important constraint, as it controls water solubility, and thus viscosity, and pressure estimates can also be used to infer magma storage depths. Temperature is a key

parameter when estimating timescales of magmatic processes based on diffusion models (e.g., Costa et al., 2020). In addition, petrological data can provide information on magmatic processes like mafic recharge, magma mixing, assimilation and fractional crystallisation (e.g., Knesel et al., 1999; Ruprecht et al., 2012; Cassidy et al., 2015; 2016).

Past studies place some constraints on the structure of the upper-crustal magma storage system at Krakatau. Mandeville et al. (1996a) proposed that the 1883 eruption was fed from a chemically and thermally zoned magma reservoir at 5 to 8 km depth. From the analysis of co-existing iron-titanium oxides, Mandeville et al. (1996a) inferred that a rhyodacite magma (880-890°C) overlay progressively hotter dacites (890-913°C), and andesites (980-1000°C). Fugacity of oxygen was estimated by the same method for rhyodacitic pumice at -10.79 to -11.07 log fO_2 (or approximately 0.96 to 1.43 above nickel-nickel-oxide (NNO) buffer; assuming pressure at 100 MPa). Dahren et al. (2012) used petrological and seismic techniques to analyse the structure of the plumbing system beneath Anak Krakatau, the post-caldera volcano that in 1927 emerged above sea-level within the 1883 Krakatau caldera. They concluded that the contemporary and 1883 plumbing systems were likely to have been subject to comparable structural controls, based on compositionally similar phenocrysts. From mineral data, they inferred that magmas stalled in three lithologically-controlled zones: 23 – 28 km (plagioclase cores), 7 – 12 km (clinopyroxene) and 3 - 7 km (plagioclase rims). The only constraints on pre-eruptive magmatic water contents come from analysis of volatiles by difference of glass inclusions, at 4 +/- 0.5 wt% (Mandeville et al., 1996a). In this study, we provide further constraints on critical magmatic storage conditions (temperature, pressure, H_2O content, fO_2) prior to the 1883 eruption.

There is still debate regarding the main triggers involved at various stages of the 1883 eruption. Potentially important processes include (i) fractional crystallisation, potentially leading to “second boiling” (Camus et al., 1987; Mandeville et al., 1996a), (ii) magma mixing (Francis and Self, 1983; Self and Wohletz, 1983) and (iii) phreatomagmatism, which has been proposed as a trigger for the

main explosions on the morning of 27th August (Verbeek, 1884). Self and Rampino (1981) ruled out phreatomagmatism as they found no textural evidence for interaction of the magma with water during fragmentation. Verbeek (1884) reported two distinct ash compositions that were erupted during May 1883: dacite and a high-alumina basalt (Stehn 1929). This led Francis and Self (1983) and Self and Wohletz (1983) to suggest that magma mixing triggered the initial stage of the Krakatau 1883 eruption. Several studies have noted the presence of rare, banded pumice clasts from the main phase of the eruption (e.g., Self and Rampino 1981), which is often used as an indicator for magma mixing (Sparks et al., 1977; Andrews and Manga, 2014; Rossi et al., 2019). However, the two visually distinct glasses are of very similar chemical compositions (Self, 1992). Camus et al. (1987) and Mandeville et al. (1996a) suggested that fractional crystallisation was the most important process prior to the 1883 eruption, increasing the SiO_2 content of the residual melt and enriching it in volatiles. Both factors make an eruption more likely and potentially more explosive (Blake, 1984). A final process recognised for the 1883 and contemporary Krakatau system is assimilation of crustal material (Gardner et al., 2012). Using mineral and whole rock Sr isotope data, Gardner et al. (2013) showed that evolving basaltic andesite (Anak Krakatau) to rhyodacite (1883 compositions), required 45% crystallisation, accompanied by assimilation of 5-23% carbonate or quartzo-feldspathic siltstone.

This study aims to integrate the known eruptive progression at Krakatau in 1883 – based on historical accounts – with new studies of the stratigraphy, crystal zoning and glass geochemistry. The new exposure of pyroclastic sequences from the 1883 eruption by the tsunami generated by the flank collapse of Anak Krakatau in December 2018 (Grilli et al., 2019; Novellino et al., 2020), means that it is possible to build significantly on prior work (e.g., Self, 1992; Mandeville et al., 1996a). Whole-rock and matrix glass data were collected and analysed in the context of this sequence and help to constrain the chemical structure of the plumbing system, allowing the magma reservoir zonation hypothesis to be tested. Thermodynamic modelling using Rhyolite-MELTS (Gualda et al., 2012), provides further insight into the role of fractional crystallisation prior

to the 1883 eruptions. Chemical analyses of both plagioclase and pyroxene phenocrysts at higher spatial resolution than previous studies (e.g., Mandeville et al., 1996a) allow the crystal growth history to be constrained in more detail. Furthermore, thermobarometric and hygrometric models provide improved constraints on magmatic conditions. These field observations, geochemical and petrological data shed new light on this highly active caldera system, and provide new context for the monitoring of the present-day activity of Anak Krakatau, as well as providing broader lessons applicable to other similar systems globally.

2. Geological Context

2.1 Tectonic setting

The Krakatau complex comprises four islands: Panjang, Sertung, Rakata, and Anak Krakatau (Figure 1). Panjang and Sertung are remnant islands left behind after a caldera-forming eruption prior to that in 1883; Rakata is the southern remnant of a pre-existing larger island that lay between Panjang and Sertung, the northern two thirds of which was destroyed in 1883 (dashed line, Figure 1). Prior to the 1883 caldera collapse, this main island of Krakatau consisted of three volcanic centres aligned NNW: Perboewatan, in the north, Danan, in the centre, and Rakata forming a higher peak to the south (Figure 1). Anak Krakatau is the current subaerial volcanic cone, which first emerged above sea-level in 1927 on the same alignment as the 1883 vents, and lies between the positions of Perboewatan and Danan.

The Krakatau archipelago is part of the Sunda Arc; volcanism in this region is caused by subduction of the Indo-Australian Plate beneath the Eurasian Plate (Figure 1). Krakatau lies in the Sunda Strait, between Java and Sumatra, at the intersection of a NNE trending lineament of Quaternary volcanic edifices roughly perpendicular to the Java trench (Nishimura et al., 1992) and a fault connecting Krakatau with the Sunda Graben (e.g. Harjono et al., 1989). The Sunda Strait is extending, as Sumatra rotates relative to Java (Ninkovich, 1976; Hall and

Spakman, 2002; Hall, 2012). Therefore, magmatism in the Sunda Strait is not only a function of subduction, but also of rifting and extension (Harjono et al., 1989) associated with slab-thinning and mantle upwelling beneath Krakatau (Abdurrachman et al., 2018).

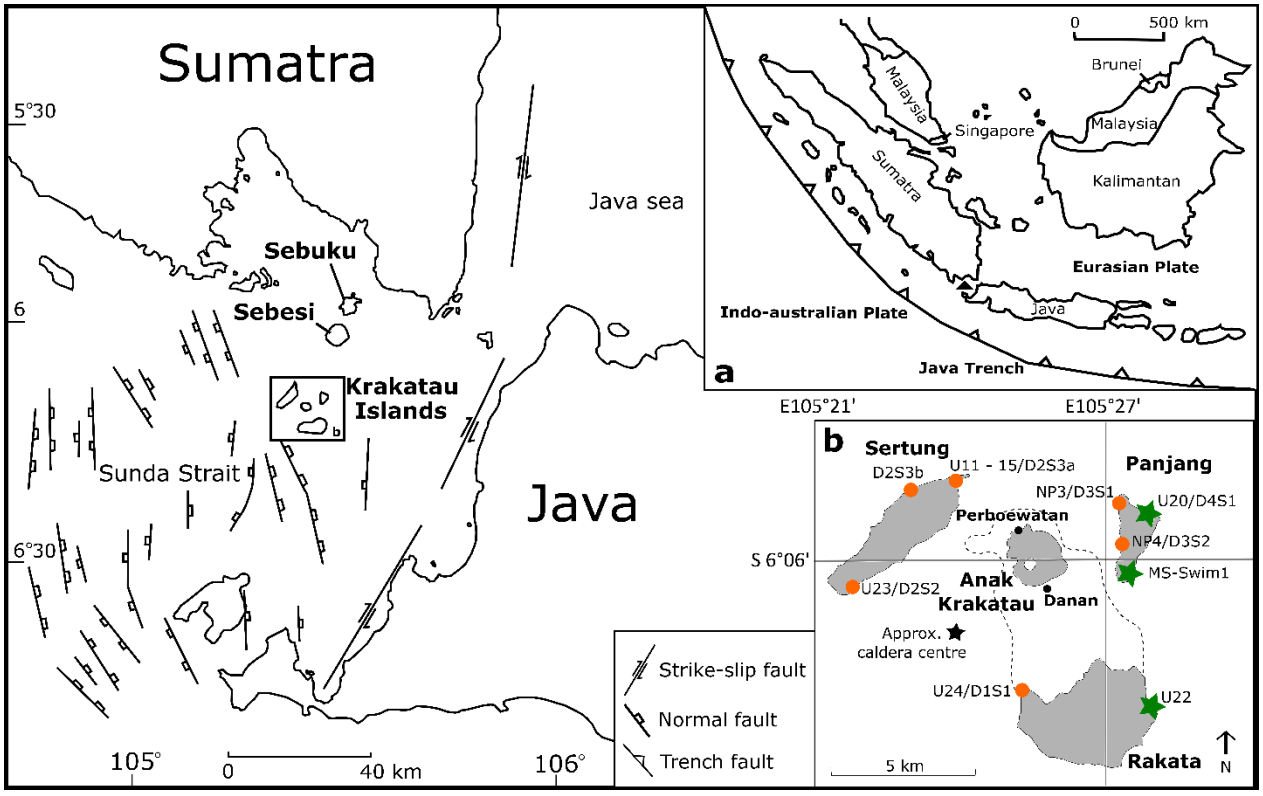

Figure 1: Tectonic map showing the Sunda Straits, with insert (a) showing the Java trench and (b) showing the Krakatau islands and field sites visited. The green stars in insert (b) are new field sites, presented here for the first time, whereas localities matching, or very close to, the orange circles were also visited by Self and Rampino (1986) and/or Mandeville et al. (1996b). Localities with two names were visited in both field campaigns (2017 and 2019). All sites visited in 2019 had considerably more exposure than observed and/or presented previously, due to erosion by the 2018 tsunami associated with a flank collapse on Anak Krakatau. The black star labelled approx. caldera centre marks the deepest part of the caldera structure, estimated from bathymetric data from Deplus et al. (1995). The dotted line represents the island prior to collapse in 1883, with Perboewatan and Danan, the 1883 active cones, marked as black circles. Figure based on Mandeville et al. (1996b), Schlüter et al. (2002), Lunt et al. (2009), Susilohadi et al. (2009) and Dahren et al. (2012).

2.2 Pre-1883 eruptive history

The ages of pre-1883 eruptions are uncertain. Drill core data suggests an eruption in the Sunda Straits at ca. 60 ka, however this cannot be definitively attributed to Krakatau (Ninkovich, 1979). The Javanese chronicle Pararaton, or the Book of Kings, describes a very large eruption, with "heavy rains of stone" in 416 AD originating from the straits of Sunda (Symons et al., 1888). However, no geological evidence presented to date substantiates this eruption. In May 1681, observations of earthquakes and pumice were made in the diaries of Johann Wilhelm Vogel and Elias Hesse, likely pertaining to an eruption of Krakatau (Vogel, 1690; Hesse, 1690; Hesse, 1694; Verbeek, 1884).

2.3 1883 Eruption

The eruption of Krakatau volcano on 26th and 27th August 1883 was the culmination of at least four months of unrest (Figure 2). The climactic eruption ejected 18 – 21 km^3 of dominantly rhyodacite ejecta (9 – 10 km^3 dense rock equivalent; Self and Rampino, 1981) in a sequence of pyroclastic density currents (PDCs) that swept across the straits of Sunda, causing volcanogenic tsunamis. In total there were approximately 36,000 fatalities (Self, 1992). This eruption resulted in the destruction of two-thirds of the main island of Krakatau, forming a submarine caldera, which manifests today as a 250 m deep depression in the seafloor (Deplus et al., 1995). The soundwaves produced from the eruption were the greatest ever recorded in the audible range (Gorshkov, 1959), and the atmospheric effects were seen around the world, with vivid sunsets observed up to a year after the eruption (Symons et al., 1888).

The first record of the 1883 eruption of Krakatau is for 20th May, with contemporary descriptions suggesting Vulcanian to Sub-Plinian activity from Perboewatan (Verbeek, 1885), which declined after 22nd May (Symons et al., 1888). Self (1992) suggested that this precursory

eruption column reached 20 km, with ash fall up to ~375 km away. There are no records of activity between 23rd and 26th May (Symons et al., 1888). On 27th May a party visited the island and observed explosions every 10 minutes (Verbeek, 1885). While there are no specific records from 28th May to 19th June, Krakatau was reported to have continuously expelled "smoke" throughout June according to the newspaper *Javasche Courant*, and Symons et al. (1888) report no interruption in activity "according to reports from lighthouses… and vessels". Krakatau began to "smoke heavily" again on 19th June (Simkin and Fiske, 1983) (Figure 2).

On 24th June, a second column of "smoke" was observed from Java for the first time, likely emanating from Danan. This coincided with the reported disappearance of the summit of Perboewatan (Symons et al., 1888). However, Ferzenaar, who was the last person to set foot on the island on 11th August prior to the climactic phase of the eruption, instead reported that Danan had partially collapsed (Verbeek, 1885). The few records that exist suggest that activity continued to fluctuate. Verbeek (1885) observed "no ash" but "a hazy red glimmer" on 3rd July, interpreted to be lava extrusion, and Symons et al. (1888) reported "continued eruptions, earthquakes and occasional violent explosions" throughout July.

Plinian activity began on 26th August (Figure 2). At 2pm local time, a black eruption column rose ~ 26 km into the atmosphere, with explosions every 10 minutes (Sturdy, 1884). By 3pm, explosions were heard ~ 670 km away (Symons et al., 1888), and the first abnormal sea wave was recorded in Batavia (modern-day Jakarta; Latter, 1981). By 5pm explosions were heard all over Java (Symons et al., 1888). There was intense volcanic lightning through the night and a strong sulphurous smell was reported on nearby ships, such as the Charles Bal (Sturdy, 1884).

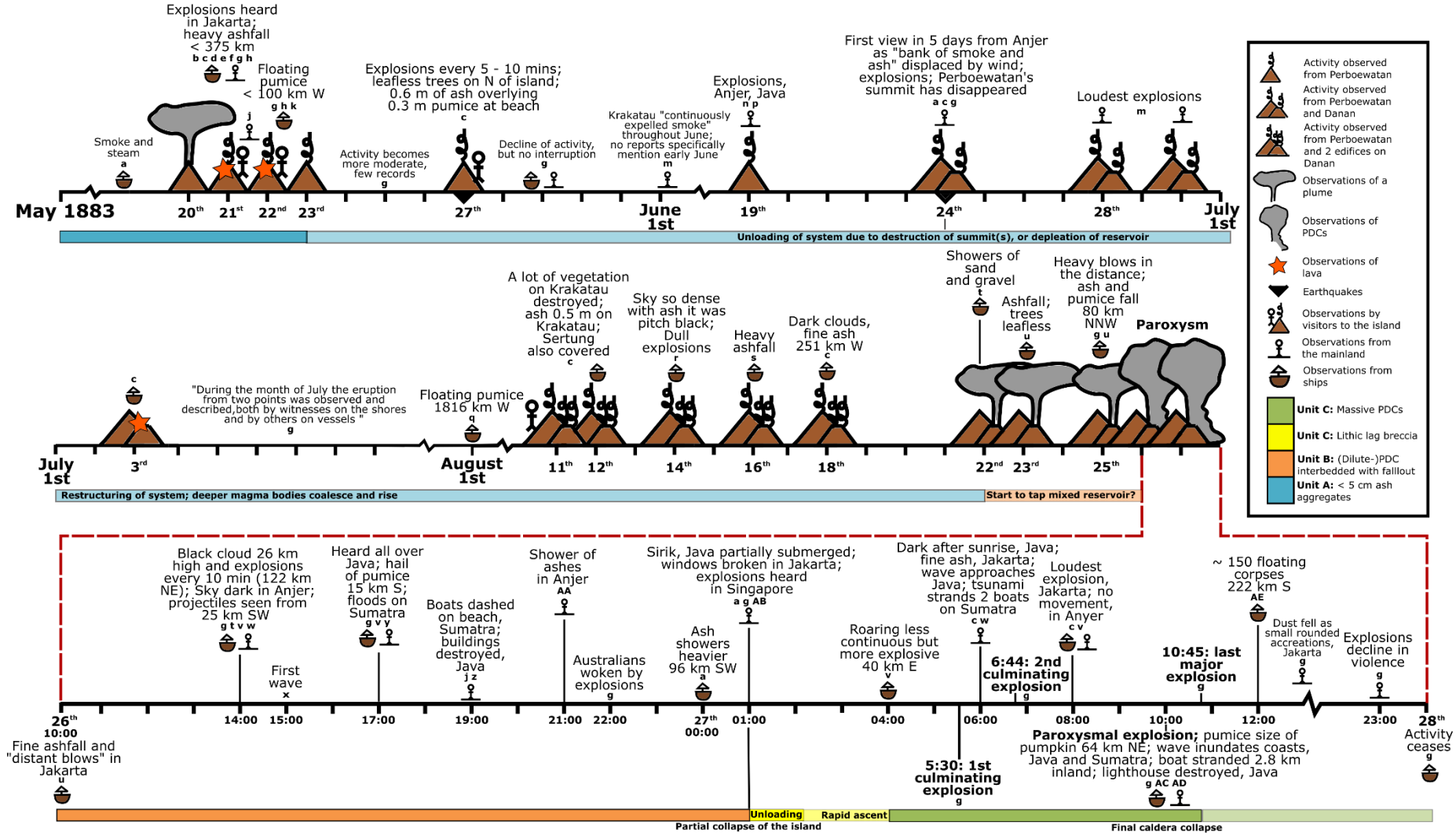

Figure 2: Schematic diagram showing the timeline of the eruption as given by various eye witness accounts. The accounts from which the information is taken is represented by letters, as follows: (a) Tenison-Woods (1884), (b) Times of London 03/06/1883, (c) Verbeek (1885), (d) Captain Walker 16/06/1883, (e) MacKenzie, Java Bode 30/05/1883, (f) Tagliche Rundchau (1883), (g) Symons et al. (1888), (h) Grainger, Algmeen Dagblad 23/05/1883, (j) Furneaux (1964), (k) Sulzer, Java Bode 30/05/1883, (m) Javasche Courant, 20/07/1883, (n) Algemeen Dagblad, 20/06/1883, (p) Algemeen Dagblad, 26/06/1883, (q) Ashdown (1883), (r) Bataviaasch Handelsblad, 16/08/1883, (s) Algemeen Dagblad, 17/08/1883, (t) Joly (1885), (u) van Heerdt, report in Royal Society archives, (v) Sturdy (1884), (w) Metzger (1884), (x) Latter (1981), (y) Algemeen Dagblad, 11/09/1883, (z) Algemeen Dagblad, 05/09/1883, (AA) Bataviaasch Handelsblad, 09/09/1883, (AB) Algemeen Dagblad, 27/08/1883, (AC) Ceylon Observer 06/09/1883, (AD) Algemeen Dagblad, 03/09/1883, (AE) Times of London, 08/10/1883.

Interpretations regarding the eruptive progression have been made from this, and then has been combined with information of the 4 units in the 1883 eruptive deposits. Page numbers for more accessible sources for historical references (Macleod, 1884; Joly, 1885; Verbeek, 1885; Symons et al., 1888; Furneaux, 1964; Simkin and Fiske, 1983) can be found in Supplementary Material 1. Note that not all tsunami timings have been included, due to limited space.

The most powerful explosions, based on pressure deviations recorded on the Batavia gasometer record (Latter, 1981), occurred at 5.30 am, 6.44 am, ~10:00 am and 10.45 am on 27th August (Symons et al., 1888); the third of these was the most violent, and was heard 850 km away in Singapore (Strachey 1888). Multiple tsunami waves traversed the Sunda Straits from the 26th to 27th August and caused the majority of casualties (Symons et al., 1888). The largest of these waves originated at approximately 10 am on 27th August (Verbeek, 1885; Latter, 1981), broadly coinciding with the most powerful recorded explosion. The whole of the northern portion of the island disappeared into the sea during caldera formation (Lindemann, 1884). However, the precise timing of caldera collapse has not yet been determined (Self, 1992). Details of historical sources are summarised in Supplementary Material 1.

2.4 Anak Krakatau

In 1927 Anak Krakatau, or "child of Krakatau", emerged above the sea surface, forming a new subaerial volcanic cone (Stehn, 1929). This soon became a permanent island, which has grown rapidly. Since the 1960s, when the active vent stopped interacting with seawater, Anak Krakatau has predominantly erupted effusively, punctuated with Vulcanian and Strombolian explosions (Abdurrachman et al., 2018).

A period of elevated activity from July to October 2018 culminated in the collapse of the southwestern portion of Anak Krakatau on December 22nd 2018. This created a volcanogenic tsunami which greatly impacted the coast along the straits of Sunda, killing 437 people (Grilli et al., 2019; Novellino et al., 2020).

3. Methods and material

3.1 1883 Stratigraphy and samples

Field campaigns to the Krakatau islands were undertaken in September 2017 and August 2019. Some field locations, originally described by Self and Rampino (1981) and Mandeville et al. (1996b), were revisited (Figure 1b). The 2019 field campaign provided new constraints on the stratigraphic sequence, as erosion associated with the December 2018 tsunami increased exposure of the 1883 sequence considerably at all localities. Stratigraphic logs were created from field observations, and cross correlated using lithological and stratigraphic characteristics, as well as glass chemistry.

In addition to samples collected on both field campaigns, three archived samples from the British Geological Survey (BGS) were analysed: two from the mail steamer Norham Castle (08 and 72), which was 92 km from Krakatau in the Sunda Straits on 26th and 27th August 1883, and one sample of ash from "Districts of java opposite Krakatau and on volcanic island itself" (07). Field locations and sample details are presented in Analytical Data 1 in the published dataset Madden-Nadeau (2020).

3.2 X-ray fluorescence (XRF)

A selection of samples collected through the 1883 stratigraphy were analysed for whole-rock major and minor element chemistry by X-Ray Fluorescence (XRF) at the Department of Geology, University of Leicester on a PANalytical Axios Advanced XRF spectrometer. Most of these samples were powdered pumice clasts, except for one sample comprising fine ash aggregates (U22.2), and four samples of bulk tephra, containing both ash and pumice. For the pumice analyses, multiple clasts were powdered from a single sample and analysed in a single aliquot.

Major and minor elements (SiO_2, TiO_2, Al_2O_3, Fe_2O_3, MnO, MgO, CaO, NaO_2, K_2O, P_2O_5 and SO_2) and Loss on Ignition (LOI) were determined on fused glass beads prepared from ignited powders, while trace elements (As, Ba, Ce, Co, Cr, Cs, Cu, Ga, La, Mo, Nb, Nd, Ni, Pb, Rb, Sb, Sc, Se, Sn, Sr, Th, U, V, W, Y, Zn, Zr) were determined on pressed pellets.

3.3 Scanning electron microscope (SEM)

Back-scatter electron (BSE) images of plagioclase and pyroxene phenocrysts and matrix glass picked from crushed pumice samples and mounted in resin blocks, were obtained with an FEI Quanta 650 field emission gun (FEG) scanning electron microscope (SEM) in the Department of Earth Sciences, University of Oxford, and a Zeiss Merlin Compact FEG-SEM at the Sir William Dunn School of Pathology, University of Oxford. Operating conditions were 20 KeV with a 15-micron aperture.

3.4 Electron Probe Microanalysis (EPMA)

Phenocryst phases were analysed on a FEG CAMECA SX-5 electron microprobe at the Department of Earth Sciences, University of Oxford. Sodium was always analysed first with a 10 s peak count time, to prevent Na migration.

Compositional profiles (n = 56) for Al, Si, Na, Ca, K, Fe, Ti, Mn and Mg were collected by Electron Probe Microanalysis (EPMA) for plagioclase phenocrysts at 15 kV acceleration voltage and 20 nA beam current, with 5-micron defocussed beam size. Point spacings in line analyses were approximately 10 microns. Points were also analysed for BSE image calibration for anorthite content with the same operating conditions. Plagioclase phenocrysts were picked from archived ash collected at the time of the eruption (BGS samples), as well as samples collected in the field. Phenocrysts were picked from samples of multiple crushed, cm-scale

pumices, one ash sample, one sample of ash aggregates and two bulk tephra samples containing both pumice and ash.

Compositional profiles for pyroxene phenocrysts picked from archived ash collected at the time of the eruption (BGS samples; n = 46) were obtained at 15 kV, with a focused beam of 20 nA for Al, Si, Na, Ca, Fe, Ti, Mn, Cr and Mg. Fe/Ti oxides (n = 419) partially included into the rim of pyroxene phenocrysts and in contact with the melt from both archive and field samples, were also analysed as points under the same conditions.

Point analyses of matrix glass, mounted in resin, were analysed on a Jeol JXA-8200 electron Microprobe in the School of Archaeology, University of Oxford. Glass analyses were conducted at 15 kV with a 5-micron defocussed beam of 6 nA for Al, Si, Na, Ca, K, Fe, Ti, Mn, Mg, P and Cl. Secondary standards of a similar composition to the target glass were analysed to check the accuracy of the calibration (see Supplementary Material 2). Most matrix glass analyses were obtained from grains picked from multiple crushed, cm-scale pumices, however two samples contained only ash, one ash-aggregates, and one was bulk tephra sample, containing both pumice and ash. Multiple pumices were crushed per sample, and glass clasts were picked and mounted from crushed material. We also analysed a sample of crushed obsidian, and three samples taken from large glassy blocks at D2S2/U23. For each sample, analyses are based on at least two clasts, except for D1S1.2 and U23.7 where the only viable analyses came from the same clast.

3.5 Vesicularity and crystallinity

Thin sections of pumice were used to estimate phenocryst content of the 1883 samples through the stratigraphy. Five images per sample were photographed through a transmitted light microscope, and crystals were traced by hand using image processing software to provide

an average estimate of crystallinity reported on a vesicle-free (VF) basis. An example of a pictomicrograph used is in Supplementary Material 3. Average vesicularity of the 1883 samples was estimated from BSE images (five to nine grains imaged per sample), picked from crushed samples, and thresholded using image processing software (e.g., Burgisser et. al., 2010). Estimates for vesicularity are likely to be slightly underestimated, as a result of plane of section effects.

Error will also be incurred as a result of the degree of user-defined thresholding chosen for each BSE image, and differences in how phenocrysts are traced by hand. Repeat measurements of thresholding and crystal tracing was carried out 10 times on a single image, averaged over 5 images, to give a 1 σ error in crystallinity estimates of +/- 0.1 %, and in vesicularity of +/- 2.5 %.

3.6 BSE image calibration for Plagioclase

Back scatter electron (BSE) intensity profiles of plagioclase phenocrysts were calibrated for anorthite content using quantitative point analyses obtained by EPMA following the approach outlined by Ginibre et al. (2002). Most phenocrysts were calibrated individually where enough EMPA data was available, whilst a global calibration was used for other crystals where brightness and contrast settings on the BSE images made the images comparable. Global calibrations were only used where $R^2 > 0.8$ for the correlation between anorthite and grey scale, determined using imageJ.

4 Results

4.1 Fieldwork and stratigraphy

The stratigraphic sequence of the 1883 eruptive deposits has previously been established by Self and Rampino (1981) and Mandeville et al. (1996b), however, the significantly increased exposure of deposits in coastal cliffs following the 2018 tsunami made this worth revisiting. The stratigraphy as presented by Self (1992) (after Self and Rampino, 1981) and Mandeville et al. (1996b), is shown in Figure 3. Terminology for deposits pertaining to pyroclastic density currents (PDCs), and particularly dilute-PDCs, has been subject to some ambiguity. Here, we use the terms PDC deposit to refer to any unit with characteristics consistent with flow-driven transport and sedimentation; and we use the term dilute-PDC deposit specifically for those PDC units which show cross stratification and are generally finer-grained and better sorted, following Branney and Kokelaar (2002). Previous authors have used the terms ignimbrite to refer to PDC deposits with more massive or poorly sorted characteristics, and surge deposits for those with dilute-PDC deposit characteristics. However, when discussing stratigraphic descriptions of previous authors we use their original terminology.

4.1.1. Previous work

Self and Rampino (1981) reported that the proximal stratigraphy comprised sub-Plinian fall deposits interbedded with surge (i.e., dilute-PDC) deposits up to 20 m thick, overlain by up to 55 m of massive ignimbrite (i.e., PDC deposit). Mandeville et al. (1996b) reported a layer of olive- to bluish-grey, fine-ash fall deposit up to 4 cm thick at the base of the 1883 deposit, which overlies a soil horizon on West Rakata and West Panjang (equivalent to our localities U24/D1S1 and NP3/D3S1, respectively). They attributed this to phreatomagmatic activity in May to August 1883. Next in the

sequence, Mandeville et al., (1996b) reported 5 - 20 cm of coarse, light-grey pumice fall deposit, followed by 4 to 6 m of fall deposits interbedded with surge deposits. At the top of the stratigraphy, Mandeville et al. (1996b) report thick accumulations of massive pyroclastic flow (i.e., PDC) deposits. The thickness of the fall deposit layer is therefore disputed, with Self and Rampino (1981) observing fall deposits interbedded with surges up to 20 m thick, and Mandeville et al. (1996b) observing up to 6.2 m of fall deposit interbedded with surge deposits.

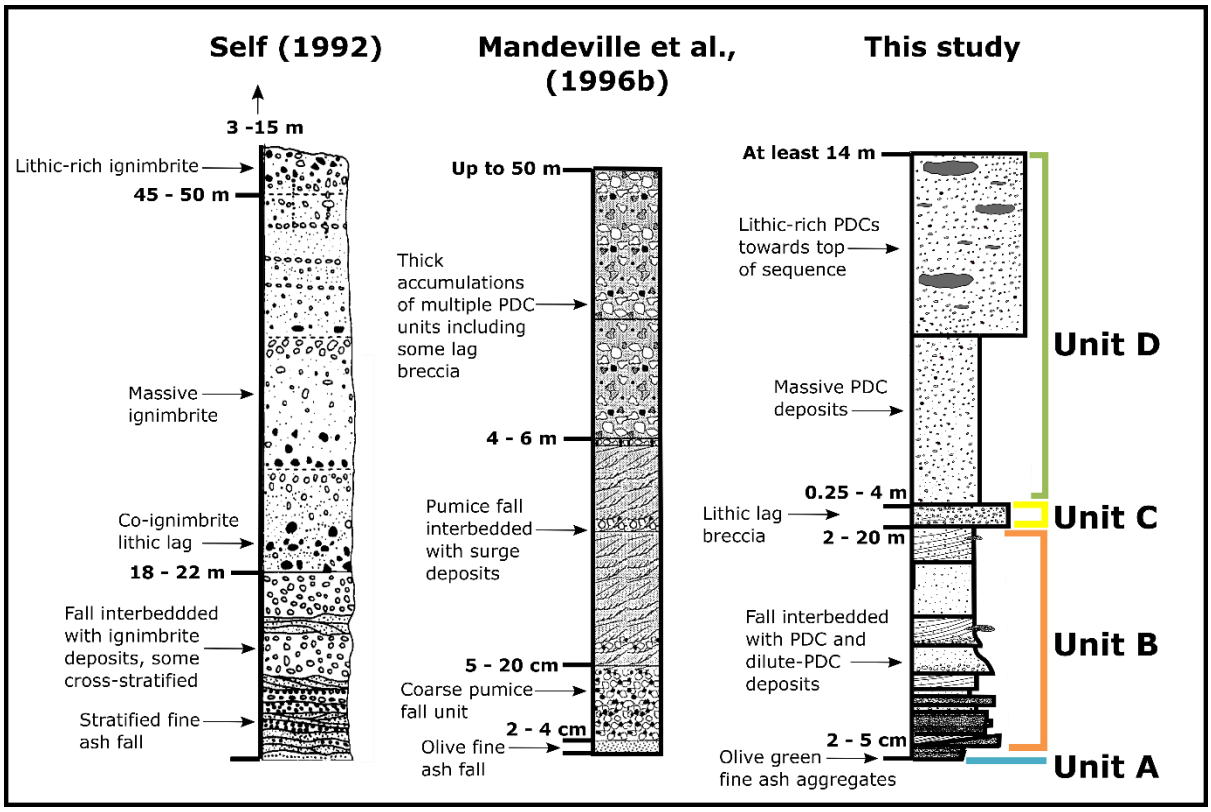

Figure 3: Composite logs of stratigraphy derived by Self (1992), Mandeville et al., (1996b) and this study. Thicknesses are for individual units, and are not cumulative.

4.1.2. This study

We present our new composite stratigraphy in Figure 3; field logs, stratigraphic correlations and field photographs for each locality are shown in Supplementary

Material 4 – 11. Like Mandeville et al. (1996b), we found a distinctive olive-green ash fall deposit at the base of the sequence (Figure 3), which we term Unit A (Figure 3; 4a). Unit A is between 2 and 5 cm thick and was only found exposed on West Rakata and South Panjang. This layer overlies a red paleosol, and is composed of fine-ash aggregates. A back-scatter electron image of the ash aggregates can be found in Supplementary Material 12.

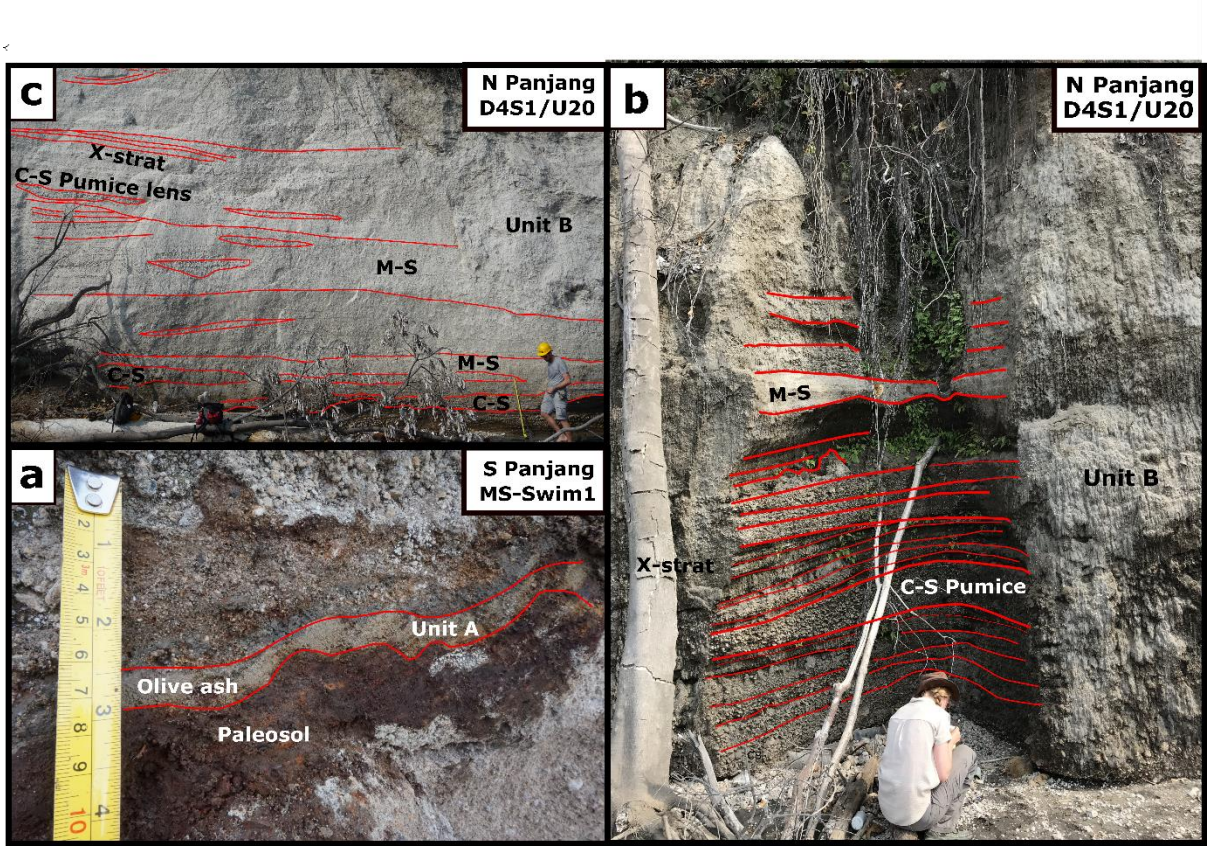

Figure 4: Panel (a) shows Unit A, as observed from locality MS-Swim1 on South Panjang, which is a thin layer of olive-green ash aggregates, overlying a red paleosol. Panel (b) shows the base of Unit B at locality D4S1/U20 on North Panjang, which is composed of clast-supported (C-S) fallout layers, interbedded with dilute-PDC deposits that show cross-stratification (X-strat). Panel (c) shows the units overlying those in panel (b), at the same locality (D4S1/U20). These are also part of Unit B, and show matrix-supported (M-S) dilute-PDC deposits interbedded with pumice-supported lenses. All locations are shown in Figure 1. People (b) or measuring tape (a and c) for scale; measuring tape is 1 m in (c).

Unit B is characterised by well-sorted beds of angular lapilli, interbedded with poorly sorted layers which are matrix-supported (Figure 4b; 4c; 5a). Clasts within the well-sorted layers are predominantly juvenile pumice (>80%), the remainder being dense, angular, and visibly altered volcanic lithics; Mandeville et al. (1996b) determined that the majority of these lithics are basalt and basaltic andesite. Of the juvenile clasts, ~90% are white pumice, although pink, grey and yellow pumice are also observed. Clasts within the poorly sorted units show similar proportions. Some of the poorly sorted beds are cross-bedded, and interpreted as dilute-PDC deposits (after Branney and Kokelaar, 2002). These dilute-PDC deposits also contain laterally restricted, discontinuous lenses of well-sorted, sub-rounded, pumiceous lapilli. Unit B is interpreted to comprise fall deposits interbedded with PDC and dilute-PDC deposits. We find that Unit B is up to 20 m thick, in agreement with observations made by Self and Rampino (1981) (Figure 3). Charcoal and tree moulds were found towards the base of Unit B at two localities. Carbonised logs were also reported by Mandeville et al. (1996b), but not attributed to a specific unit within the stratigraphy.

Next in the sequence is Unit C, which is characterised by lithic blocks (up to 50 cm) in a poorly sorted, juvenile matrix (Figure 5a; 5b). This section of the sequence is interpreted to be a lithic lag breccia (Druitt and Sparks, 1982; Branney and Kokelaar, 2002). Both Self and Rampino (1981) and Mandeville et al. (1996b) identify lithic lag breccias in the sequence (Figure 3), however only Self and Rampino (1981) used them as a correlating horizon. The lag breccia is variable in stratigraphic thickness (0.3 to 4 m), and bifurcates in some outcrops (Figure 4a). The proportion of lithic blocks within this unit also varies between localities.

Unit D is a massive, poorly sorted, matrix-supported unit containing predominantly pumice clasts (80-90% of clasts) in an ash-rich matrix (Figure 5b). Both Self and Rampino (1981) and Mandeville et al. (1996b) identify a similar unit towards the top of the sequence (Figure 3). The structureless nature of Unit D suggests it was likely deposited by large volume, high-concentration PDCs. Another characteristic feature of Unit D is the presence of obsidian clasts. Frothy, glassy, and banded obsidian clasts are present (e.g., Shields et al., 2016), making it likely that the obsidian is juvenile (Self and Rampino, 1981). Rare black and white banded pumices, as reported by Self and Rampino (1981), were also observed.

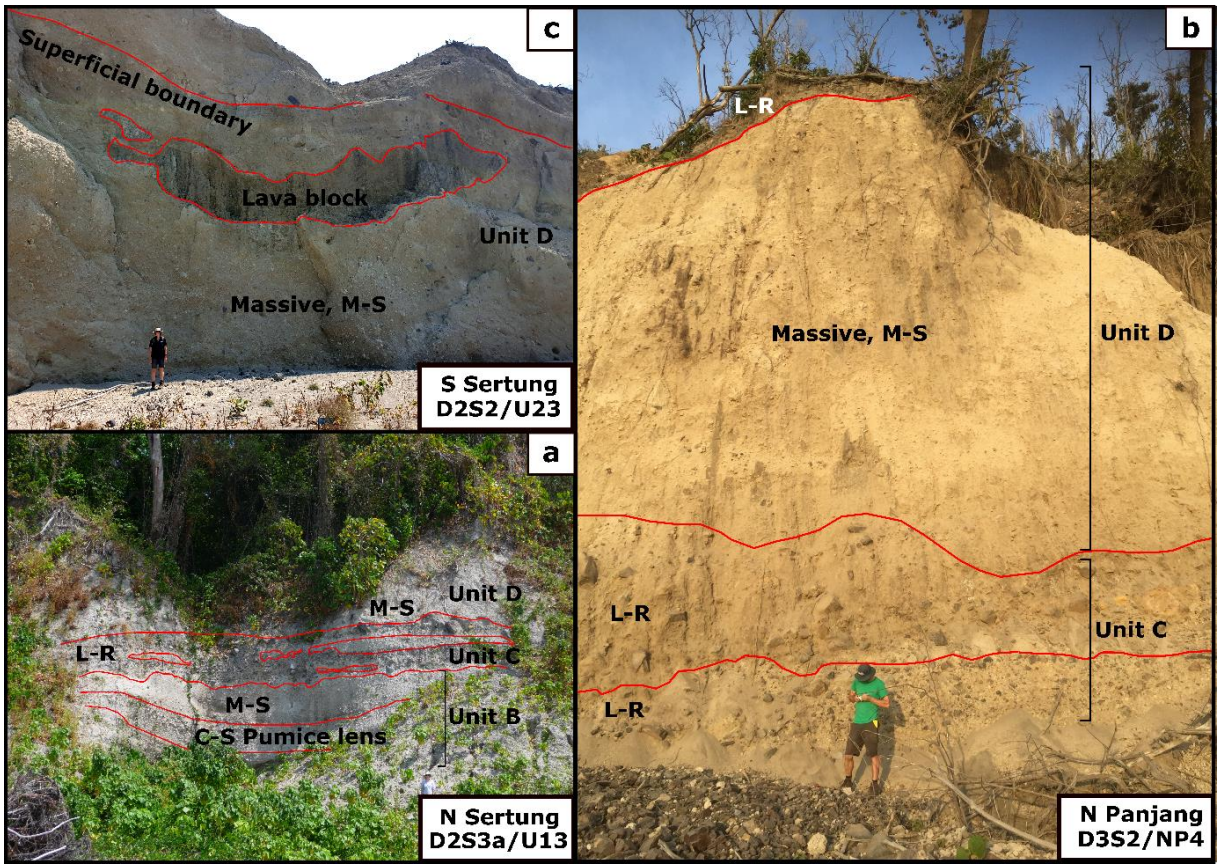

Figure 5: Panel (a) shows Units B, C and part of Unit D, as observed from locality D2S3a/U13, North Sertung. Unit B comprises clast-supported (C-S) pumice layers interbedded with matrix-supported (M-S) layers. Panel (b) shows Units C and D at locality D3S2/NP4, North Panjang. Unit C in both panels (a) and (b) show lithic-rich (L-R) layers. Panel (c) shows the top of Unit D at locality D2S2/U23, South

Sertung. Unit D is comprised of massive PDC deposits in both panels (b) and (c). In panel (b), there is a second lithic-rich layer at the very top of the sequence. In panel (c) there are large, glassy blocks up to 8 m in size. All locations are shown in Figure 1. People for scale.

A second lithic lag breccia horizon is observed at the top of Unit D on North Panjang (Figure 4b), which concurs with an updated stratigraphic log presented by Self (1992) (Figure 3). New exposure on South Sertung (D2S2/U23, Figure 1), observed for the first time in the August 2019 field campaign, contains large glassy blocks up to 8 m in length within the massive PDC unit (Figure 5c). Although the blocks are intact, they are intensely fractured and have sub-rounded irregular shapes, aligned broadly horizontally, but not confined to a single horizon within the deposit (Figure 4c). Some of these fractured blocks are black in colour and vitreous, and look similar to the smaller obsidian clasts already identified by Self and Rampino (1981), with a low phenocryst content, whereas other blocks are dull grey in colour, with a higher phenocryst content (comparable to pitchstone). Their geochemistry will be discussed further in section 4.5. This section of Unit D also contains clasts of mudstone. We also noted crude horizontal stratification of the PDCs delineated by subtle colour changes; this was also observed in massive PDC units described by Mandeville et al. (1996b).

Locality U22 (Figure 5) is the only outcrop where the entire sequence (Units A to D) can be observed. The sequence appears to be condensed (2.8 m), and we use this as a type locality. Key marker beds in the 1883 stratigraphic sequence include: a thin, green, ash-aggregate layer overlying a red paleosol at the very base of the sequence, delineating Unit A (Mandeville et al., 1996b; Figure 3; 6a); Pumice fallout units interbedded with PDC and dilute-PDC deposits (Self and Rampino, 1981; Figure 3), some of which contain charcoal aligned east-west (Unit B; Figure 6b); the lithic lag

444 breccia overlying Unit B (Unit C; Figure 6c); and Unit D, consisting of massive PDC
445 deposits containing obsidian (Self and Rampino, 1981; Mandeville et al., 1996b; Figure
446 3) (Figure 6c). Figure 7 shows the logs from each locality cross-correlated by unit.

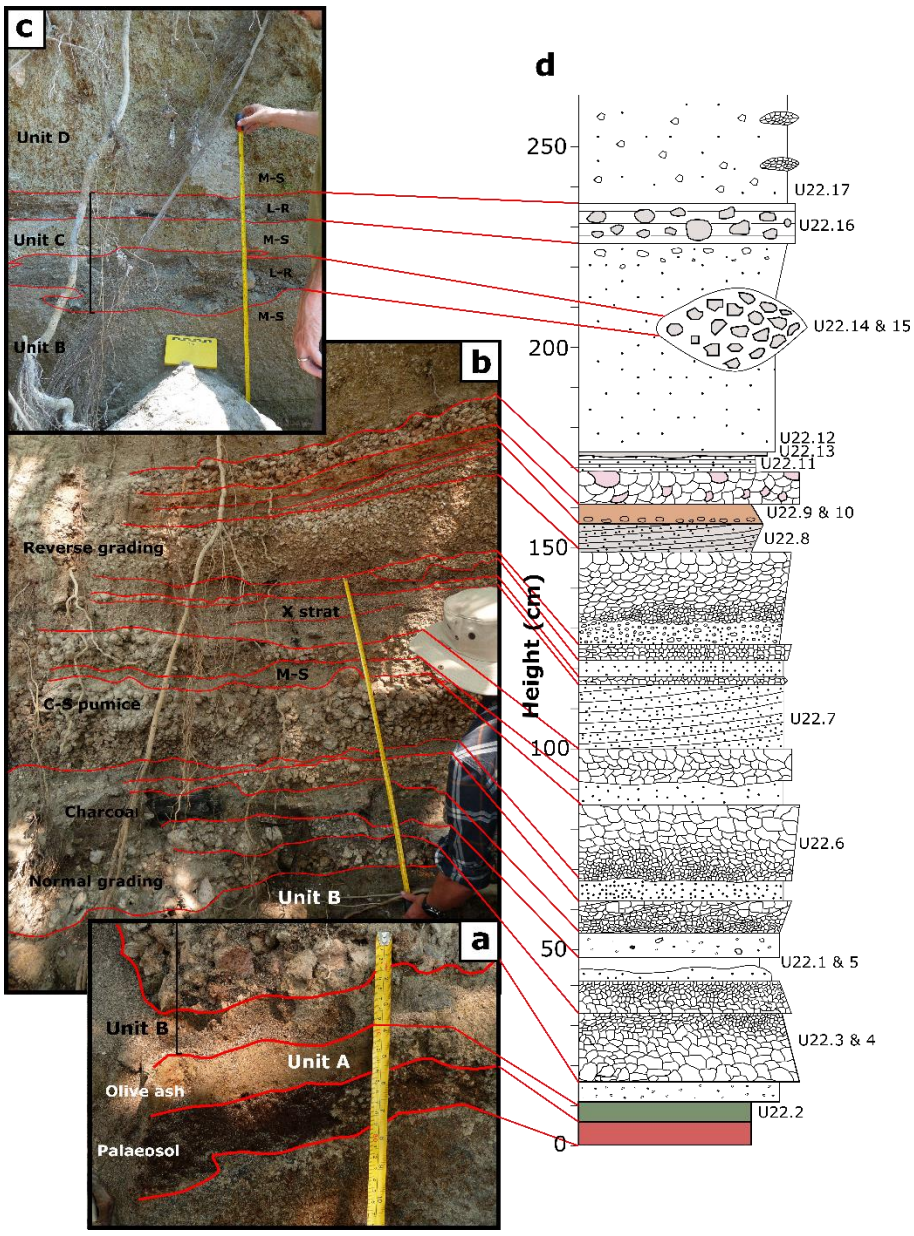

447

448 **Figure 6:** Photographs and log of deposit at locality U22 to show the entire sequence (E.
449 Rakata; location shown in Figure 1). Panel (a) shows Unit A at the base of the sequence, (b)
450 shows Unit B, (c) shows Units C and D, and (d) shows the cross correlated stratigraphic log,
451 with sample numbers down the right-hand side. C-S stands for clast-supported, X-strat for

cross-stratification, M-S for matrix-supported and L-R for lithic-rich. Measuring tape for scale (a-c).

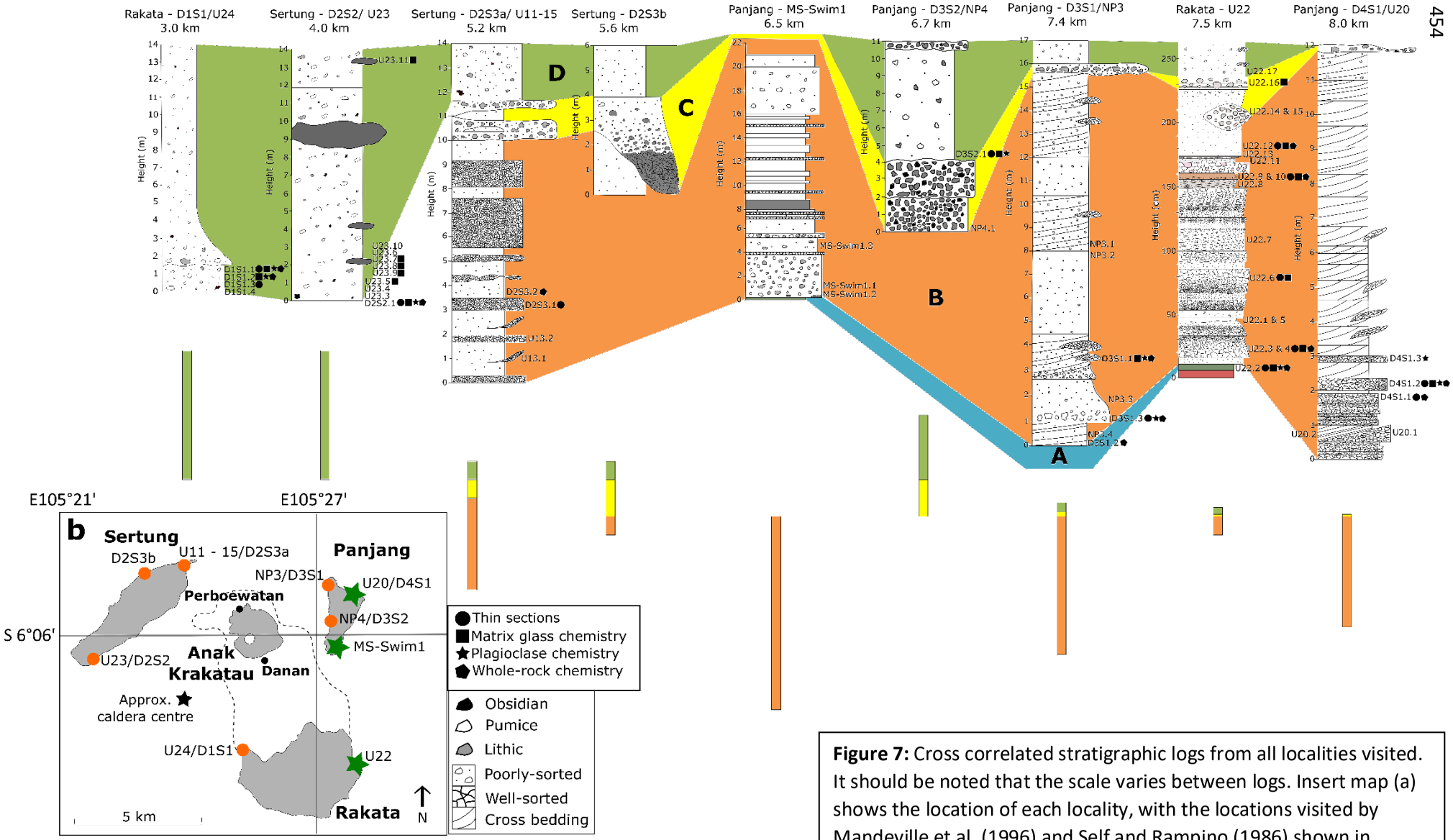

Figure 7: Cross correlated stratigraphic logs from all localities visited. It should be noted that the scale varies between logs. Insert map (a) shows the location of each locality, with the locations visited by Mandeville et al. (1996) and Self and Rampino (1986) shown in orange, and fieldsites new to this study indicated by a green star. Letters represent the discussed units, with A corresponding to blue, B to orange, C to yellow and D to green. Bars below logs represent the relative thicknesses of each unit. Symbols by sample numbers represent thin sections and chemical analyses. Distance above log is from the assumed caldera centre, taken from Deplus et al. (1995).

The spatial distribution and thicknesses of PDC (including dilute-PDC) deposits change through the stratigraphic sequence (Figure 8). Unit B is thickest to the north east, with approximately 20 m of vertical exposure (Figure 8a). Unit C appears to be more evenly distributed around the main island (Figure 8b), whereas Unit D is thickest in the south west (14 m; Figure 8c), rather than north as reported by Self and Rampino (1981). These thicknesses are based on only limited exposures, and there are only two localities where it was possible to observe the base of the sequence (MS-Swim1; south Panjang and U22; east Rakata); this will lead to underestimates of unit thickness. Self and Rampino (1981) noted a lack of fall deposits in the south west, which we confirmed.

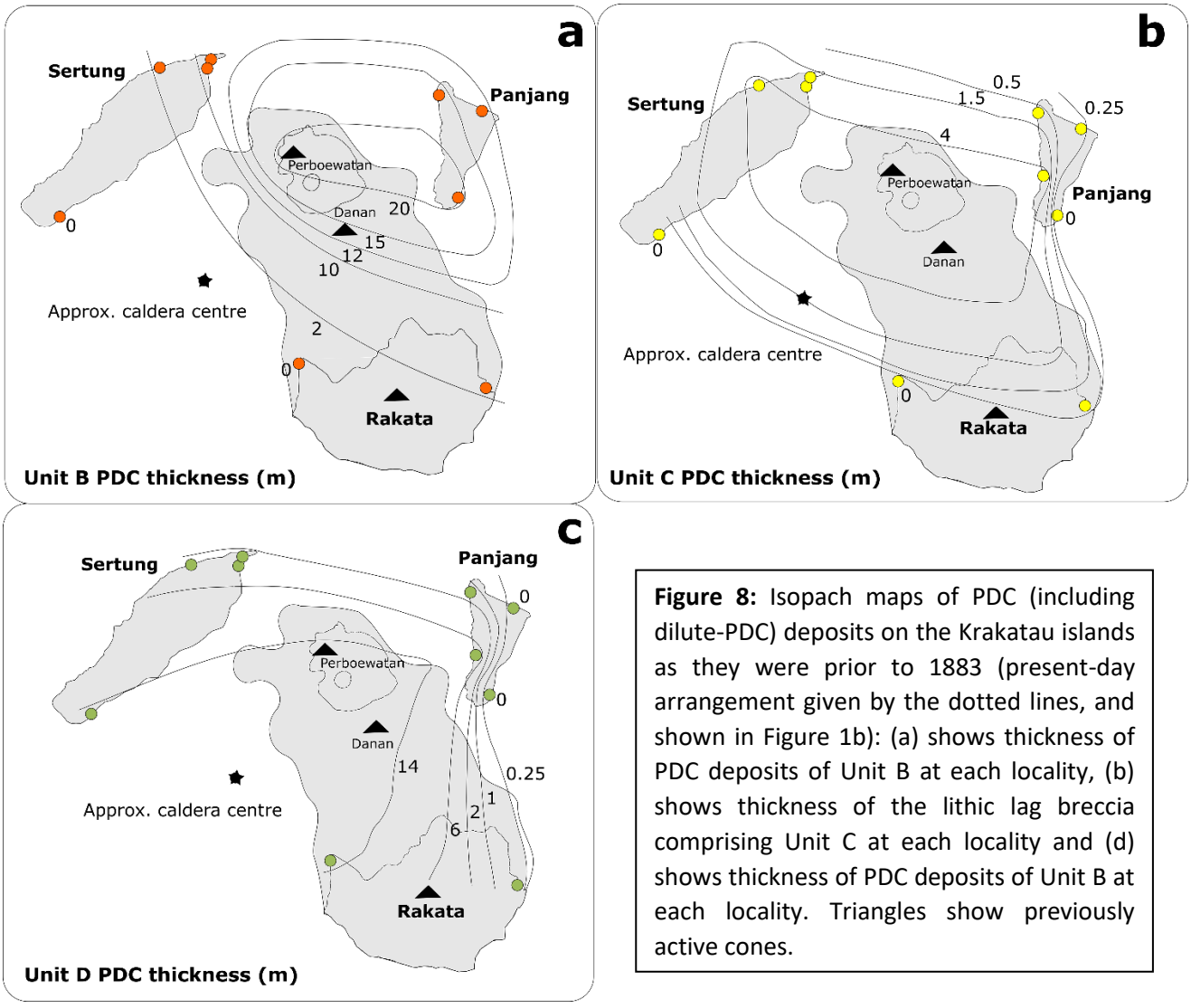

Figure 8: Isopach maps of PDC (including dilute-PDC) deposits on the Krakatau islands as they were prior to 1883 (present-day arrangement given by the dotted lines, and shown in Figure 1b): (a) shows thickness of PDC deposits of Unit B at each locality, (b) shows thickness of the lithic lag breccia comprising Unit C at each locality and (d) shows thickness of PDC deposits of Unit B at each locality. Triangles show previously active cones.

466 **4. 2 Vesicularity and crystallinity**

467 Crystallinity of juvenile clasts increase up the stratigraphic sequence. Unit A (n = 1) is
468 comprised of poorly vesicular ash aggregates, with crystallinity (on a vesicle-free
469 (VF)/porosity-free basis) at 5 %. In Unit B (n = 7), crystallinity (VF) ranges from 10 – 20 % and
470 Unit D (n = 3) has a crystallinity (VF) of 30 %. Vesciularity in both Units B and D ranges from 70
471 – 80 %.

472

473 **4.3 XRF whole-rock chemistry**

474 XRF whole-rock data are presented in Analytical Data 2 in the dataset Madden-Nadeau (2020).
475 The 1883 whole-rock samples have anomalous major element compositions compared with
476 previously reported values (Oba et al., 1982; Self 1992; Mandeville et al., 1996a; Turner and
477 Foden 2001; and Gardner et al., 2013). These samples also have high Loss on Ignition (LOI; 3.1
478 – 8 wt%). We suspect these samples have experienced seawater alteration, based on the
479 positive correlation between LOI and Na_2O (Figure 9a), and negative correlation with SiO_2
480 (Figure 9b). The values for major elements are anomalous, even after correcting for LOI, in all
481 but two of the samples, and thus cannot be used to assess the chemostratigraphy.

482 Trace element compositions show no evidence for alteration, when plotted against Zr, which
483 is a high field-strength element, assumed to be immobile (Figure 9c-f). Correlations between
484 Zr and other incompatible elements provide no evidence for loss or gain of these elements
485 during alteration, as the ratios between them remain constant. Zr vs Y (Figure 9e) has the
486 strongest positive correlation, with an R^2 value of 0.87. Once normalised to LOI to correct for
487 the dilution effect (Figure 9d and f), there is no discernible systematic correlation with
488 stratigraphic height for Ba and Y with Zr.

489

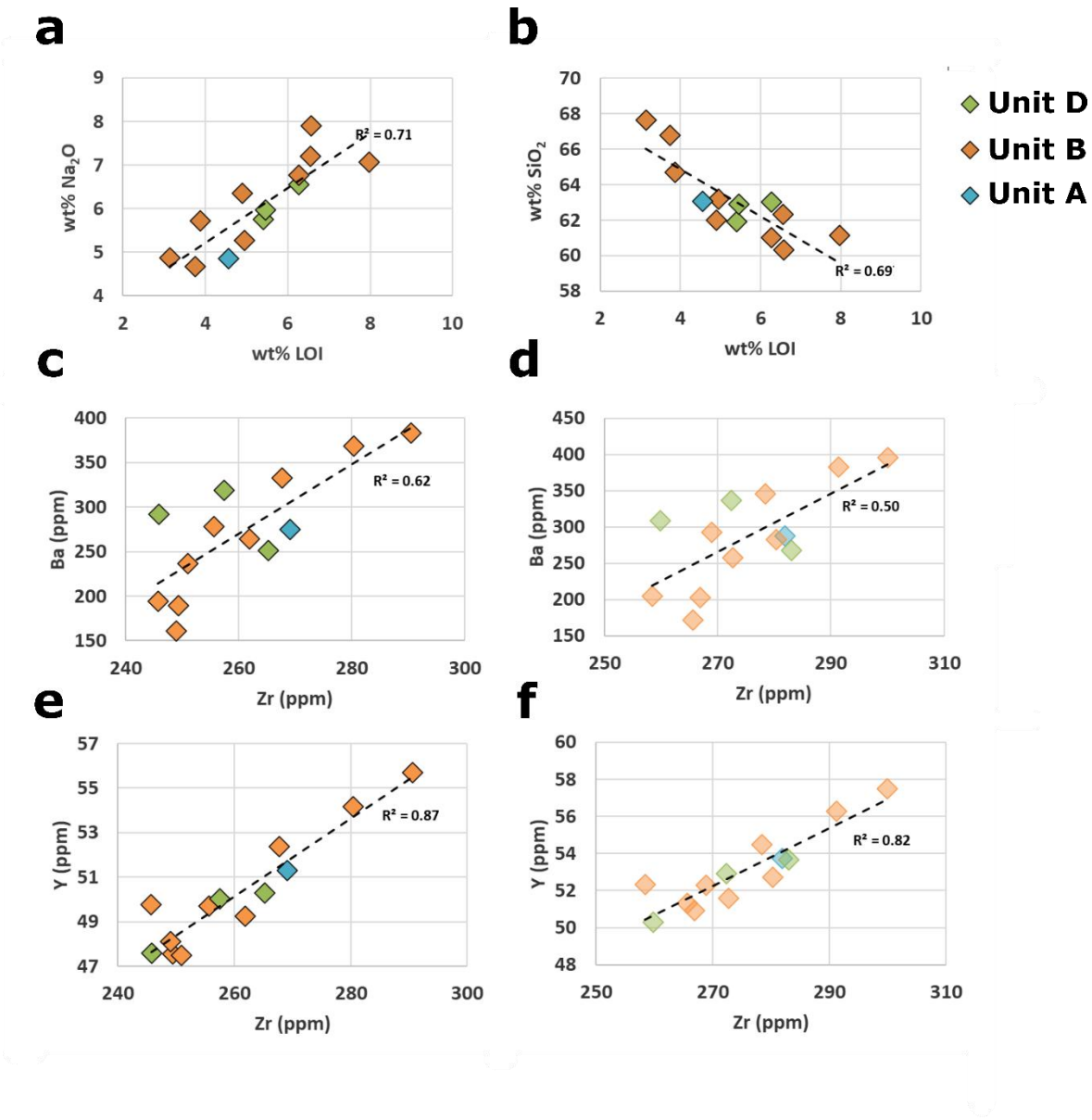

490

491 **Figure 9:** (a) a plot showing a positive correlation between LOI vs Na_2O and (b) the negative correlation
492 between LOI and SiO_2, indicating that the samples are likely to have undergone seawater alteration.
493 (c) and (d) show Ba plotted against Zr, which is assumed to be immobile, with (d) showing the data
494 corrected for LOI (transparent symbols). (e) and (f) show Y against Zr, with (f) being corrected for LOI
495 (transparent symbols). The dashed lines are the least squares linear regression, and in (c) and (e)
496 represent the constant ratio between the two trace elements, and thus no losses or gains during
497 alteration. The higher the R^2 value, the less those elements have been lost or gained during alteration.

(e) Y vs Zr has the highest R^2 value of 0.87, thus being the elements least affected by alteration, and (f) shows that there is no correlation in chemistry of Y and Zr with stratigraphic height.

4.4 Phenocryst textures and chemistry

4.4.1 Plagioclase

Plagioclase is the dominant phenocryst phase in pumice clasts throughout the 1883 eruption stratigraphy and, as is typical of subduction settings, most plagioclase crystals are zoned. When discussed here, cores and rims refer to the centre and edge of euhedral, unbroken crystals. Zoning profiles vary between crystals from very complex to unzoned (Figure 10). Anorthite (An = molar Ca/(Ca+Na)) compositions present across all sampled plagioclase phenocryst cores, ranges from An_{29} to An_{90} (mean An_{54}; 95 analysed crystals), bearing in mind that the 'core' may be subject to section effects. Phenocrysts also have a wide range in rim compositions: An_{26} to An_{65} (mean An_{48}; 77 analysed crystals) (Figure 11). There is no discernible inter-unit variation in crystal textures, or the core and rim anorthite contents. There is also no correlation between anorthite content of the rims and cores. Resorption textures are common (e.g., Figure 10a), with some crystals having patchy cores and/or zones (~ 30 %; e.g., Figure 10c). Both normal (~ 35 % of rims) and reverse zoning (~ 60 % of rims) are also common at various stages in plagioclase crystallisation histories, with ~ 5 % of crystals showing no zoning at all (Figure 10e). The anorthite content of crystals does not converge on a single value at the rims. A high anorthite (>An_{70}) core is observed in ~ 20 % of phenocrysts (e.g., Figure 10a). Due to the complexity in the plagioclase phenocryst zoning profiles, it is not possible to identify discrete typologies, or common phases of growth, as has been achieved in previous studies (e.g., Druitt et al., 2012). All whole plagioclase anorthite traverses, from euhedral rim to core, are shown on a single plot in Supplementary Material 13.

Analytical data for plagioclase phenocrysts, with accompanying BSE images, from Units B to D and archived BGS samples, can be found in Analytical Data 3 – 11 in the dataset Madden-Nadeau (2020). Analytical data for Unit A, and one Unit B sample (U22.3) can be found in Supplementary Material 14.

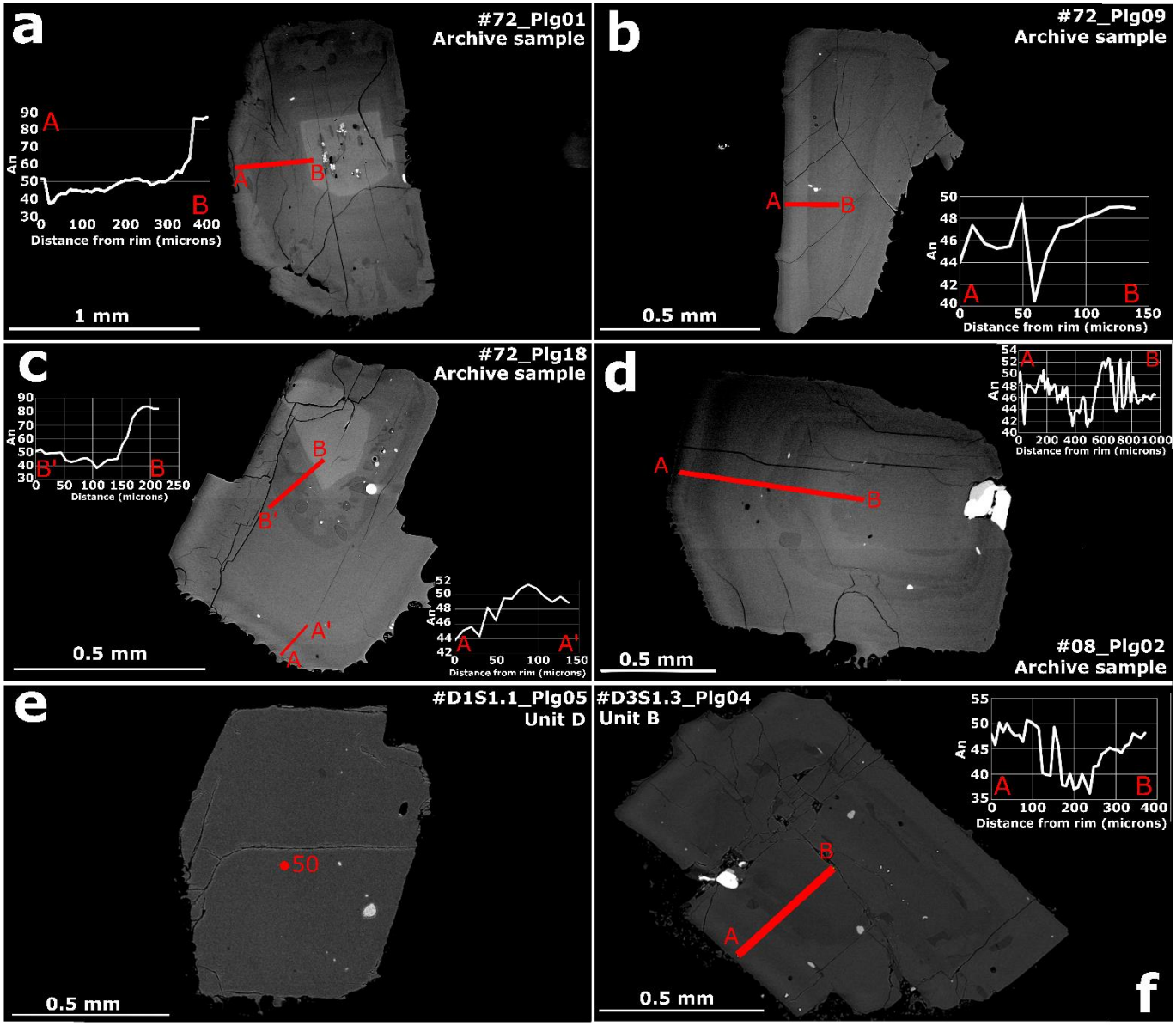

Figure 10: BSE images of a selection of plagioclase phenocrysts, with anorthite traverses shown in red. Note that the BSE grey scale differs between each image. Plagioclase (a) has a high anorthite core, followed by oscillatory zoning, resorption textures and a reverse zone at the rim; (b) has a single reverse zone between core and mantle, with normal zoning at the rim; (c) has a high An core,

followed by a patchy, reabsorbed zone, then oscillatory zoning, with normal zoning at the rim; (d) has an An_{46} core with resorption textures, followed by oscillatory zoning, with the rim being reverse zoned; (e) appears largely unzoned with consistent composition of ~An_{50} and (f) has an An_{47} core with resorption textures, followed by two reverse zones.

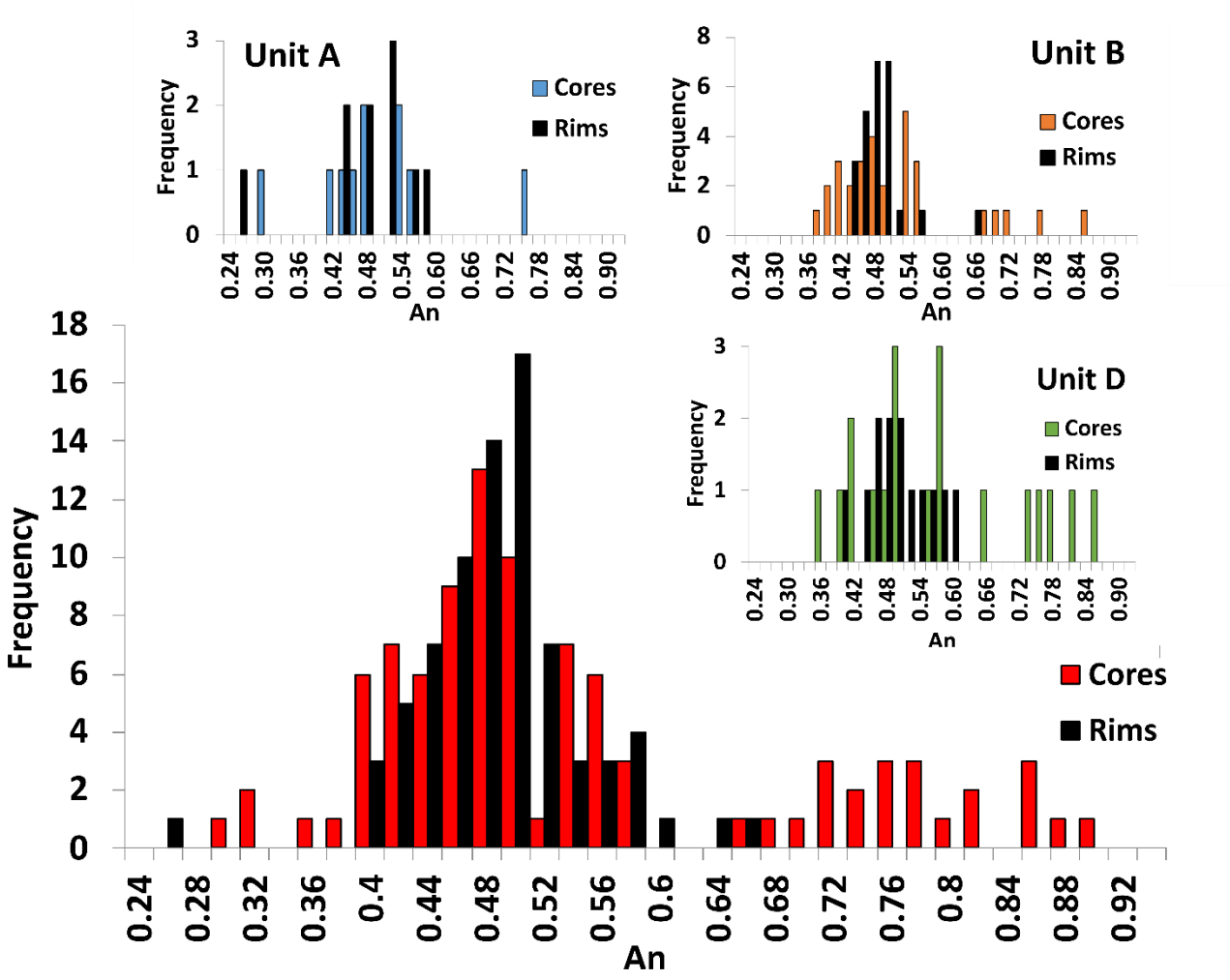

Figure 11: Histogram showing the frequency of core and rim compositions in anorthite for plagioclase phenocrysts; 97 individual crystals were used to create this histogram, taken from the 3 archive samples, as well as 4 samples from Units B, 3 samples from Unit D, and one sample from Unit A. The three inserted histograms show distributions of anorthite compositions for Unit A, B and D individually. It should be noted that there will be some error in crystal core compositions as a result

543 of plane of section effects. Not all crystals had both viable core and rim analyses, as rim analyses were
544 only included for euhedral, unbroken phenocrysts.

545

546 **4.4.2 Pyroxene and Fe-Ti oxides**

547 Pyroxene phenocrysts were picked from archived BGS ash samples, collected at the time
548 of the eruption. When discussed here, cores and rims refer to the centre and edge of
549 euhedral, unbroken crystals, and cores may be subject to plane of section effects.
550 Orthopyroxene rims and cores range in Mg# (Mg# = molar Mg/(Mg+Fe)) from 0.67 to 0.72
551 (n = 22, σ = 0.1), whilst the range for clinopyroxene is 0.73 to 0.77 (n = 23, σ = 0.1).
552 Pyroxene phenocrysts are largely unzoned in major elements. All data for pyroxene
553 phenocrysts can be found in Analytical Data 12 – 14 in the dataset Madden-Nadeau
554 (2020), and a plot showing all whole pyroxene traverses from euhedral rim to core, is
555 shown in Supplementary Material 15.

556 Fe-Ti oxides (n = 419) partially included in pyroxene rims, and in contact with the melt,
557 were analysed from Units B to D in the stratigraphy; they are magnetite and ilmenite. All
558 chemical data for Fe-Ti oxides can be found in Analytical Data 15 in the dataset Madden-
559 Nadeau (2020).

560

561 **4.5 Matrix glass**

562 Matrix glass data for the 1883 pyroclastic sequence normalised to 100 % anhydrous
563 compositions are plotted in Figure 12, with full data table in Analytical Data 16 in the dataset
564 Madden-Nadeau (2020). Totals range from 96.0 to 101.2 wt % prior to normalisation. Matrix
565 glasses from Unit A are distinct, and more evolved than the rest of the proximal 1883
566 sequence, with SiO_2 ranging from 72.6 to 74.7 wt%. Data for Units B, C and D overlap, with a

broad trend towards marginally less evolved compositions, showing a slight decrease in both $SiO_2$and total alkalis, moving up the sequence (Figure 12). SiO_2 for Unit B glasses range from 71.4 to 72.7 wt%, Unit C from 70.9 to 72.3 wt%, with Unit D ranging from 70.6 to 72.3 wt%.

Matrix glass of an obsidian clast and samples from three of the large glassy blocks on the south of Sertung (U23/D2S2.2) within Unit D were also analysed. Matrix glass from the blocks and smaller obsidian fragments are broadly similar to the matrix glass of pumice and ash ejected in the 1883 eruption, extending to more evolved compositions, with SiO_2 ranging from 71.8 to 77.6 wt% (Figure 12). Full chemical data for the matrix glass of the blocks can be found in Supplementary Material 16.

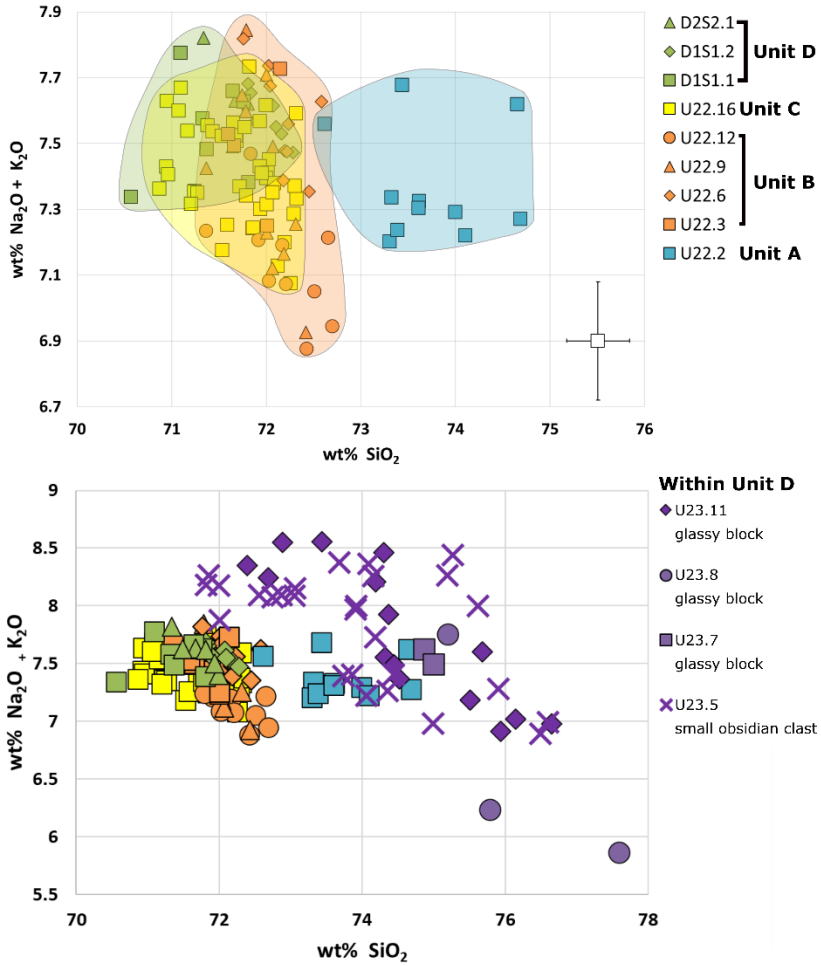

Figure 12: (a) Matrix glass data on a total alkali and silica diagram (Le Bas et al., 1986). Colours of symbols and transparent areas correspond to stratigraphic units: A = blue, B = orange, C =

yellow and D = green, as in Figure 6. Each symbol represents a separate sample, with the key in stratigraphic order. Unit A is more evolved than, and distinct from, Units B to D. Average error is given to 1 σ. (b) shows the same data, overlain with data from the glassy blocks and obsidian found within Unit D at U23/D2S2 on south of Sertung.

4.6 Thermobarometry

4.6.1 Fe-Ti oxides

Pre-eruptive temperatures and oxygen fugacities of the 1883 magmas were estimated from the compositions of titanomagnetite and hemoilmenite crystals, using the Fe^{2+}-Mg exchange model of Ghiorso and Evans (2008). Fe-Ti oxide pairs were tested for equilibrium using the Mg-Mn equilibrium line (Bacon and Hirchsmann, 1988). Fe-Ti oxides are likely to yield the last equilibration temperature before quenching (Rutherford and Devine, 1988; Geschwind and Rutherford, 1992; Lindsley and Frost, 1992).

The temperature range for all Fe-Ti oxide pairs (n = 64; 24 touching, 47 partially included within the same pyroxene phenocryst and in contact with the melt; chemical data in Analytical Data 15; dataset Madden-Nadeau 2020) was 890 to 935 ^{o}C, with a mean value of 914 +/- 50 ^{o}C. The range of temperatures generated for the 24 touching Fe/Ti oxide pairs is between 891 and 935 ^{o}C, with an average of 913 ^{o}C. The oxygen fugacity (fO_2) range for all Fe-Ti oxide pairs is 0.6 to 0.85 log units above the nickel-nickel-oxide (NNO) buffer, with the mean being NNO + 0.76. The same range of values for fO_2 is seen within the data set for the 24 touching pairs (average of NNO + 0.74). The temperatures and fO_2 of Units B, C and D all show considerable overlap. A temperature fO_2 plot can be found in Supplementary Material 17. These temperatures are interpreted as the final pre-eruption equilibration temperature.

4.6.2 Plagioclase hygrometer

Pre-eruptive dissolved water content of the melt for samples from Units A, B and D are estimated using a plagioclase-melt hygrometer (Waters and Lange, 2015) which is based on the crystal-liquid exchange reaction between the anorthite and albite components. From the anorthite contents of plagioclase rims and matrix glass data (n = 59), and the mean Fe/Ti oxide temperature (914 ^{o}C), we infer a mean H_2O content of 3.4 wt% for Unit A, 3.6 wt % for Unit B, and 3.5 wt% for Unit D. Allowing for uncertainty in Fe/Ti oxide temperatures (890 to 935 ^{o}C), gives a range of water contents from 2.6 to 4.3 wt% for all three units. These results are consistent over pressure inputs of 100 to 250 MPa. It should be noted that these are estimates of the final pre-eruptive H_2O contents, and will not reflect the entire range of conditions experienced by plagioclase phenocrysts throughout their crystallisation histories.

Equilibrium in plagioclase is difficult to test, owing to composition being a function of both temperature and H_2O content, however only anorthite compositions for plagioclase with paired liquid anorthite compositions that overlap with the compositional data for which the hygrometer was calibrated has been used to generate these estimates of water content (Supplementary Material 18).

4.7 Rhyolite-MELTS modelling

Melt evolution was modelled using Rhyolite-MELTs (Gualda et al., 2012) (Figure 13). The starting composition is the most primitive composition (4.63 wt% MgO) from Anak Krakatau analysed by Dahren et al. (2012). Initial H_2O contents of 1 – 3.5 wt% (steps of 0.5 wt%; varied between runs) were modelled isobarically. Pressure was varied between runs from 50 - 300 MPa (steps of 50 MPa). In all runs, temperature was dropped from 1200 to 700 °C in increments of 2 °C. The lines of descent that fit the best with whole-rock and

matrix glass compositions for the 1883 pyroclastic sequence were modelled at an initial H_2O content of 1.5 wt%, and lie between 125 and 250 MPa (Figure 13; dashed lines). The evolution of H_2O within the melt indicates that it is water-undersaturated prior to eruption under these conditions, as otherwise the H_2O content would have plateaued on the H_2O vs SiO_2 plot in Figure 13(f). Varying the initial water content has a much larger effect on the liquid line of descent than varying the pressure.

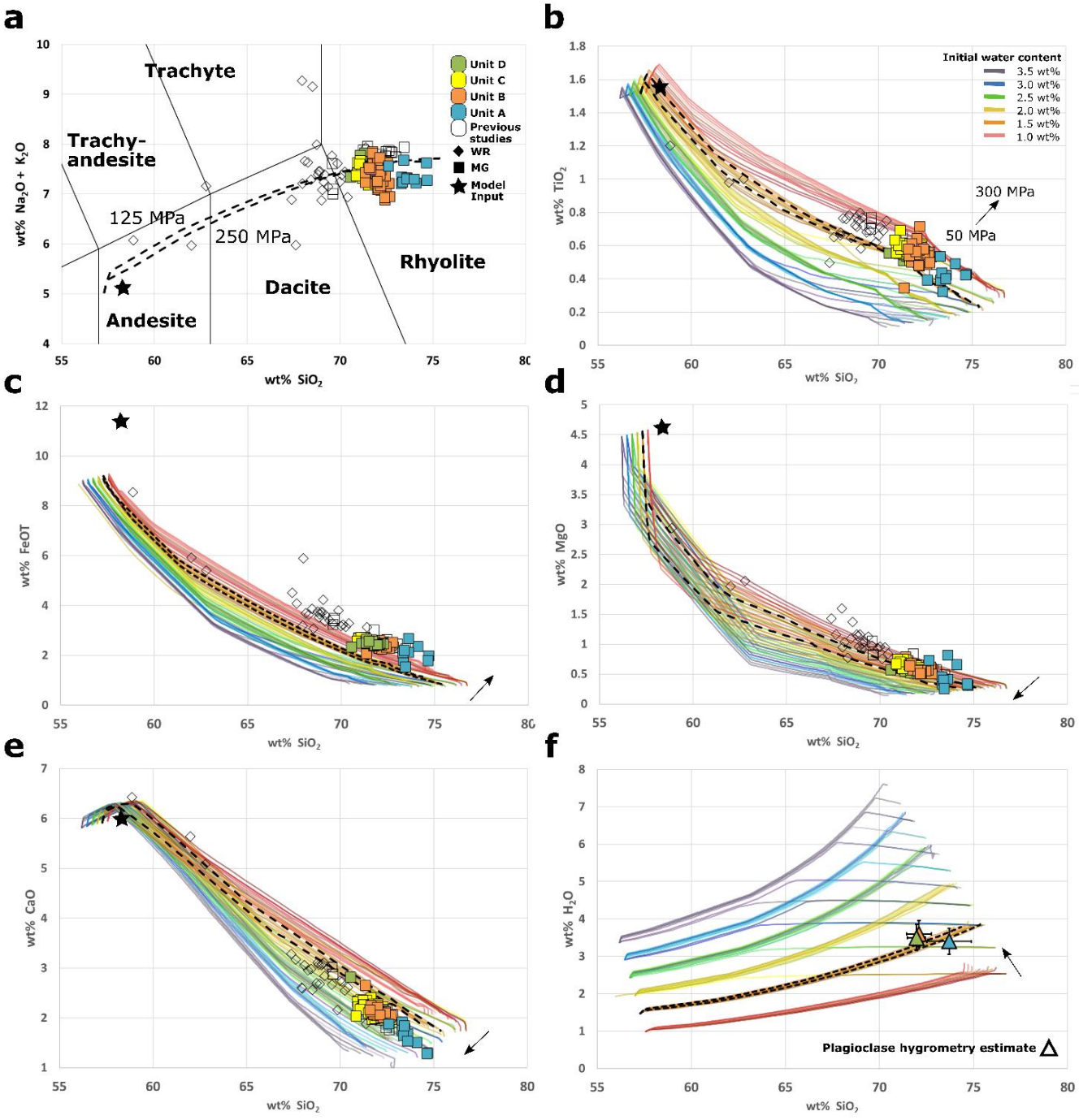

Figure 13: (a) shows a total alkali and silica diagram (Le Bas et al., 1986), and (b) to (e) show Harker diagrams containing matrix glass analyses from 1883 samples analysed in this study (MG, coloured squares), as well as matrix glass and whole rock analyses from previous studies (Colourless squares and diamonds, respectively; Oba et al., 1982; Self 1992; Mandeville et al., 1996a; Turner and Foden 2001; and Gardner et al., 2013). Colours denote the different stratigraphic units, as presented in Figure 7. Matrix glass data are all normalised to 100 % anhydrous. Liquid lines of descent are shown, modelled

isobarically in Rhyolite-MELTS (Gualda et al., 2012), with (f) showing how H_2O content varies with SiO_2 in these models. Red lines were modelled with an initial H_2O content of 1 wt%, orange 1.5 wt%, yellow 2 wt%, green 2.5 wt%, blue 3 wt% and purple 3.5 wt%. Arrows indicate direction of increasing pressure (steps of 50 MPa from 50 to 300 MPa) between liquid lines of descent modelled at the same initial water content (same colour). The effect of varying the initial H_2O content in these models is much greater than that of pressure. The dashed lines were modelled at 125 MPa and 250 MPa, with an initial H_2O content of 1.5 wt%, and liquid lines of descent that fall between these lines provide best estimates of the conditions under which the 1883 melt evolved. The input composition is indicated by the star and is from Anak Krakatau (Darhen et al., 2012). The triangles in (f) indicate H_2O contents of the average melt composition for Units A, B and D, as modelled using plagioclase hygrometry (Waters and Lange, 2015) using the average temperature generated by Fe/Ti oxide thermometry (914 ^{o}C; Ghiorso and Evans, 2008). Standard error of 0.35 wt% is indicated by the error bars, along with 2 σ of the average SiO_2 content. Where the lines flatten in (f) represents water saturation of the melt at the corresponding pressure.

5 Discussion

5.1 Structure of plumbing system

The structure of the pre-eruption magma plumbing system remains a key unknown, and yet an understanding of the reservoir architecture is critical to assessing long-term volcanic hazards (Edmonds, 2008). The lack of systematic change in trace element chemistry with stratigraphic height (Figure 9) is not consistent with the postulated existence of a single chemically zoned, and sequentially tapped, magma reservoir at shallow depths, as suggested previously for the 1883 system (Mandeville et al., 1996a; Gardner et al., 2013), and contrasts with the prominent chemical zonations recognised in the deposits of some other large

666 magnitude explosive eruptions, such as the Green Tuff, Pantelleria and the Bishop Tuff,
667 California (Williams et al., 2014; Hildreth and Wilson, 2007).

668 Fe-Ti oxide temperatures reported by Mandeville et al., (1996a), based on the Anderson and
669 Lindsley (1988) model, were interpreted as evidence for a stratified magma reservoir, with
670 homogenous rhyodacite (880-890 °C) overlying dacite (890-913 °C), and andesite (980-1000
671 °C). However, the more mafic components form only a minor constituent of the erupted
672 volume (~ 6 %), and there is no evidence that their frequency varies with stratigraphic height.
673 We also found no evidence for these lower silica compositions as a juvenile melt component
674 in the samples analysed in this study. Our Fe-Ti oxide temperature estimates, outlined in
675 section 4.6.1 and based on the Ghiorso and Evans (2008) model, show no variation with
676 stratigraphic height from Units B to D, with an average final equilibration temperature of 914
677 °C and a narrower range than previously reported (890 to 935 °C). The lack of systematic
678 variation in temperature with stratigraphic height is not consistent with the existence of a
679 simply zoned magma reservoir.

680 The diverse and heterogeneous populations of plagioclase phenocrysts, which display a large
681 range of crystallisation histories over the entire stratigraphic sequence (Figure 10 and 11), is
682 not easy to reconcile with a zoned magma reservoir. Patchy cores/zones are observed in 30%
683 of crystals, however some have higher anorthite compositions and show resorption (e.g.,
684 Figure 10c), while others show the reverse (e.g., Figure 10a). Plagioclase rim compositions
685 vary between An_{26} to An_{65}, with no clear modality, indicating a spectrum of different
686 crystallisation conditions, and requiring crystals to have been mixed only shortly prior to
687 eruption to prevent their rims from equilibrating (Figure 11). Normal zoning of rims accounts
688 for 35 % of crystals, with 60 % being reverse zoned; there is no convergence towards a single
689 anorthite content, as might be expected from simple homogenisation of two or more discrete
690 magma compositions. Unzoned phenocrysts account for 5% of the population (e.g., Figure

10e). This variability in the phenocryst population is inconsistent with a simple zoned magma reservoir, and instead suggests that these phenocrysts grew under a range of different conditions until shortly before eruption.

The matrix glass in Unit A is chemically distinct and more evolved than the rest of the sequence (Figure 12; with the exception of the Unit D glassy blocks, discussed below), indicating the presence of a more silica-rich, and likely shallower melt-rich region that was erupted first. The matrix glass SiO_2 contents for Units B to D (Figure 12) show subtle compositional differences with stratigraphic height, with B presenting slightly more evolved compositions and spanning a wider range of total alkali contents than Units C and D. The broad compositional consistency means that the melt present throughout the shallow system was likely of similar bulk compositions, with the variations in total alkali content (Figure 14a) within the 2 sigma error. The subtle trend towards a slightly more homogenous and less evolved melt is more consistent with syn-eruptive mixing of chemically similar melts, than a large-scale zoned reservoir.

Our rhyolite-MELTS modelling suggest that the shallow magma system lies at 125 – 250 MPa (Figure 13), equivalent to approximately 5 to 10 km within the crust, consistent with the 5 – 8 km depths estimated by Mandeville et al. (1996a) from plagioclase melt barometry (Housh and Luhr, 1991). At present-day Anak Krakatau, Dahren et al. (2012) inferred that crystallisation of plagioclase and two pyroxenes takes place at 4 to 8 km, suggesting that the depth range of the pre-2018 magma plumbing system is little different from that of 1883, due to lithological controls on reservoir formation; these depths are corroborated by seismic tomography data (Jaxybulatov et al., 2011; Harajono et al., 1989).

In contrast to the complex and varied zoning profiles observed in the plagioclase phenocryst population (Figures 10 and 11), which suggests that they grew under a variety of conditions, pyroxene phenocrysts lack strong zoning. Muted zoning in pyroxene phenocrysts would

716 therefore either suggest consistent magmatic conditions for growth, or that the crystals were
717 resident in hot magma long enough for diffusion to smooth out their zoning profiles.

718 To determine whether the zoning in pyroxene phenocrysts was smoothed out via time-
719 dependant diffusion, we can estimate diffusion timescales for pyroxene and plagioclase from
720 the 1-dimensional diffusion equation:

721 $$x = \sqrt{(Dt)}$$

722 where *x* is the mean diffusion length, D is the diffusion coefficient and *t* is time. We have
723 chosen to investigate Mg diffusion, as Mg zoning is present in plagioclase but is considerably
724 muted in pyroxene. Given a diffusion coefficient for Mg in clinopyroxene ($5x10^{-21}$ m^2s^{-1};
725 Schwandt et al., 1998), it would take centuries for diffusion to homogenise a length scale of
726 order 10 microns. When the above diffusion equation is applied to plagioclase, for the same
727 temperature, over the same distance, using the Mg diffusion coefficient given by LaTourrette
728 and Wasserburg (1998) of $7.19x10^{-18}$ m^2/s, the timescales are in the order of months to years.
729 Therefore, both plagioclase and pyroxene phenocrysts could not have been resident in a hot
730 magma for sufficient time to smooth the Mg profiles in the pyroxene population, as significant
731 Mg variations in plagioclase are retained. This implies that diffusion is unlikely to be the cause
732 of the discrepancy in zoning complexity between the two crystal populations.

733 The compositional consistency in matrix glass (Figure 12) and pyroxene phenocryst chemistry
734 means that the complex crystallisation histories recorded by plagioclase are therefore likely
735 to reflect variations in magmatic conditions e.g., P_{H2O}, temperature, fO_2, rather than melt
736 composition. Plagioclase crystallisation is more sensitive to these changes in magmatic
737 conditions than other phenocryst phases (e.g., Mollo et al., 2011), meaning that, in a system
738 where the melt composition was similar but other conditions varied, plagioclase could record
739 complex crystallisation histories, whilst pyroxene remain largely unzoned. One hypothesis for
740 generating varied magmatic conditions would be the existence of multiple, discrete melt-rich

741 regions of similar composition. To investigate the crystallisation histories in more detail, and
742 test this hypothesis, automated processing of a much larger sample of phenocrysts could be
743 used to identify common growth zones, and events within plagioclase zoning profiles (e.g.,
744 Cheng et al., 2017; Probst et al., 2018).

745 The presence of anorthite-rich (An_{70} to An_{92}) plagioclase cores in 20 % of plagioclase
746 phenocrysts (e.g., Figure 10a) likely indicates the existence of a deeper, more mafic reservoir
747 feeding the shallow system, as suggested by Mandeville et al. (1996a) for the 1883 eruption,
748 and Dahren et al. (2012) for the Anak Krakatau system. Highly anorthitic plagioclase may
749 reflect growth in a deeper, more mafic melt at earlier stages in the development of the
750 reservoir. The relatively homogeneous glass chemistry suggests these more mafic
751 compositions were largely erased by the time the reservoir had matured to its pre-eruptive
752 state, as the alternative would require very efficient mixing of the melt phase. The range of
753 high-anorthite plagioclase core compositions (An_{70} to An_{91}; Figure 11) indicates that they grew
754 under differing conditions (e.g., fO_2, T, P, H_2O content) within the deeper system. Sieve
755 textures in high anorthite cores, as well as strong resorption textures, followed by lower
756 anorthite mantles (e.g., Figure 11a), are most consistent with decompression (e.g., Nelson and
757 Montana, 1992; Viccaro et al., 2010), potentially during extraction from this deeper reservoir,
758 and subsequent mixing with magmas in the shallow system. The presence of a large range of
759 different crystal textures in significant proportions is also consistent with accumulation of the
760 magma body through many different episodes of mixing (e.g., El Chichón; Andrews et al.,
761 2008). The lack of significant variation in matrix glass data (Figure 12) can be explained if the
762 1883 melt is sourced from a similar host composition.

763

764

765

766 **5.2 Role of pre-eruptive fractional crystallisation**

767 The importance of fractional crystallisation processes in both the compositional evolution of
768 the magma, and in concentrating volatiles, varies greatly between volcanoes, with other
769 processes such as magma mixing often cited as eruption triggers (e.g., Sparks et al., 1977). It
770 is thus important to discuss the role of fractional crystallisation in the magmatic system prior
771 to the 1883 eruption of Krakatau.

772 Mandeville et al. (1996a) conclude that fractional crystallisation is likely to have been the
773 dominant process in the plumbing system beneath Krakatau prior to its 1883 eruption. They
774 found limited evidence for magma mixing, and an abundance of normal zoning in phenocrysts.
775 Normal zoning is a common feature in plagioclase within this dataset, and accounts for ~35 %
776 of all rims, supporting an interpretation that a proportion of phenocrysts were growing under
777 stable conditions not long before eruption.

778 Our Rhyolite-MELTS modelling (Figure 13) shows that it is possible to evolve from an Anak
779 Krakatau composition (basaltic andesite) to the 1883 melt composition by simple fractional
780 crystallisation, with a starting H_2O content of 1.5 wt%, and final water content of 3.4 - 3.6 wt%.
781 Thus, no other internal processes need to be invoked to reach the composition of the 1883
782 magmas from an Anak Krakatau basaltic andesite starting composition. Small discrepancies
783 between the model and natural samples may be as a result of the system not being entirely
784 isobaric.

785 Eruptions of silica-rich magma bodies at < 300 MPa can be internally triggered by volatile
786 saturation resulting from fractional crystallisation, without efficient degassing (Tramontano et
787 al., 2017). The modelled evolution of H_2O using Rhyolite MELTS (Gualda et al., 2014; Figure
788 13f) suggests that it is likely that the pre-1883 reservoir did not reach water saturation prior
789 to eruption, because the water content does not plateau under the best-fit pressure and
790 temperature conditions. Using VolatileCalc (Newman and Lowenstern, 2002) we model H_2O

saturation at a shallower crustal pressure of ~95 MPa (compared with best-estimates of 125-250 MPa for the 1883 reservoir), for a rhyodacite magma with 3.6 wt% H_2O at a temperature of 914 ^oC. However, over the pressure range of 125 – 250 MPa, an estimated, additional 175 – 925 ppm of CO_2 would be sufficient for the system to reach volatile saturation. These values are certainly within the range expected for arc magmas (e.g., Blundy et al., 2010), lending credence to the idea that the shallow magma system was volatile saturated prior to eruption, and that fractional crystallisation is likely to have primed the magmatic system for eruption, and is a potential trigger, if degassing was inefficient.

5.3 Role of pre-eruptive magma mixing

Recharge of magma reservoirs and magma mixing are often cited to be eruptive triggers (Sparks et al., 1977). Mandeville et al., (1996a) rule out magma mixing as a trigger for the 1883 eruption, based on a lack of reverse zoning in phenocrysts, and a low abundance of mixed pumices. However, ~60% of plagioclase phenocrysts in this study show reverse zoning at the rim, a result likely obtained by investigating crystal zoning transects at a spatial resolution of 10 microns, rather than just core and rim point analyses. It is important therefore to discuss the role that magma mixing had prior to the 1883 eruption of Krakatau.

As discussed in section 5.1, it is likely that the compositional variations in plagioclase crystals (Figures 10 and 11) represent different P, T and/or H_2O conditions, rather than differing melt composition, because the matrix glass and pyroxene phenocryst chemistry are broadly consistent. Therefore, the high proportion of reverse zoning at plagioclase rims is likely to indicate changes in magmatic conditions, rather than mixing of compositionally distinct magmas. The volume of visually mingled pumice is also small (Mandeville et al., 1996a), and not observed in Units A – C of the stratigraphy. Furthermore, the visually mingled pumices do not show compositional differences between the dark and light matrix glasses (Self 1992).

Mafic enclaves are also entirely absent within the stratigraphy. Stehn (1929) reports some mafic ash collected during the precursory eruptive phase, however evidence of this ash was not observed on either field campaign, suggesting it may not have been preserved, possibly because it is volumetrically minor component similar to the andesite glass (~1 %) reported by Mandeville et al., (1996a).

However, syn-eruptive mixing of chemically similar magmas (rather than pre- or syn-eruptive mixing of chemically distinct magmas) crystalising under different magmatic conditions, could account for the wide range in plagioclase rim compositions (Figure 10 and 11), as they would not have had time to equilibrate with the new host melt. The matrix glass compositions also support this, as they are broadly consistent, but become slightly more homogenous as the eruption progresses through Units B to D (Figure 12), which could result from mixing of chemically similar melts syn-eruption. One hypothesis might be that different melt-rich regions within the shallow system coalesced and mixed syn-eruptively as a result of magma withdrawal and system restructuring. In this case, magma mixing would be considered a consequence of magma body destabilisation during eruption, rather than an eruptive trigger (e.g., Christopher et al., 2015); this has been invoked as an explanation for homogeneity in pyroclasts coexisting with complex phenocryst zoning for similar crystal-poor caldera systems (Cashman and Giordano, 2014).

5.4 Eruptive progression

A schematic diagram illustrating the proposed evolution of the magmatic system and how this links with the eruptive progression is shown in Figure 14. Unit A (Figure 4a; 6a; 7) is comprised of a green ash aggregate fall deposit at the base of stratigraphy, which is distinct in its chemistry, being more evolved than the eruptive material that follows (Figure 12). Unit A is also volumetrically minor when compared with the overlying sequence. We concur with

841 Mandeville et al. (1996b) that Unit A likely represents the sub-Plinian May phase of the 1883
842 eruption of Krakatau. This is supported by reported observations of a maximum of 50 cm of
843 green ash at the coast in June 1883 (Symons et al., 1888). We also suggest that Unit A erupted
844 from a more-evolved, shallower melt-rich region.

845 The observation that Unit A is composed of aggregates of fine ash could indicate that the May
846 1883 activity was phreatomagmatic (Mandeville et al., 1996b). This interpretation is
847 consistent with historical accounts made by inhabitants of the nearby island of Sebesi, who
848 visited the main island of the Krakatau complex on 21st of May: “the earth burst open at their
849 feet” on the beach. European officials who travelled from Anjer the following day also
850 reported: “near the beach, the earth was belching fire and smoke” (Furneaux 1964). According
851 to these accounts, Krakatau was erupting close to the coast in May, making magmatic
852 interaction with seawater possible. This is corroborated by reports from the ship Prins
853 Hendrick, which passed close to Krakatau on 12th August: “I passed the island on the north
854 side… the new opening of the crater... appeared to be a small hole, maybe 100 ft in diameter,
855 only a few meters above sea level” (Macleod 1884). However, Ferzenaar, a visitor to the island
856 the day before, noted only subaerial vents. Brown et al., (2010) also note that ash aggregates
857 can also form in a moist atmosphere, so interaction of the magma with seawater during
858 fragmentation is not required to account for the Unit A deposits. Therefore, there is ambiguity
859 in both the evidence from deposits and the historical accounts regarding the degree of
860 phreatomagmatic character of the 1883 May phase.

861 There are periods in both early June and late July 1883 which have sparse historical records
862 (Figure 2), and it is not known whether the activity was continuous. The volcano was attracting
863 much less attention, and therefore it is at least likely that the eruptions were smaller, if not
864 less frequent. It is thus difficult to know whether any activity after 27th May contributed
865 significantly to the deposition of Unit A or not.

As discussed in section 5.3, the wide range in plagioclase rim compositions (Figures 10 and 11), and subtle changes in matrix glass chemistry throughout the stratigraphy towards a more homogenous melt (Figure 12), suggest that after the initiation of the eruption in May 1883 there was a continuing process of coalescence and syn-eruptive mixing of shallow-stored melt-rich regions. The emptying of the shallow silicic reservoir from May onwards may have promoted the restructuring and mixing of the shallow system. Partial collapse of the summits of Perboewatan or Danan from June to August (Verbeek 1885; Symons et al. 1888; Figure 2) may also have led to downward propagating stress changes in the magmatic system, aiding reorganisation of the magmatic system (e.g., Tarasewicz et al., 2012).

Our hypothesis is that magma body destabilisation occurred over the ~ 2-3 months leading up to the onset of the paroxysmal phase of the eruption. Unit B represents the onset of this climactic eruptive phase, comprising interbedded PDC and fall units (Figure 4b; 5a; 7), and tree remains (Figure 6b). The deposition of Unit B may have started as early as 22nd August (Figure 2). The increase in deposit thickness from Unit A (<5 cm) to B (up to 20 m) is likely as a result of increased eruptive flux, assuming no significant topographic changes. The increase in eruptive flux is likely to be due to vent widening, however stress changes related to the reduction in overburden on the shallow magmatic system, may have contributed (e.g., Watt, 2019).

The PDC deposits of Unit B appear to be thicker in the north east (Figure 8a), suggesting that this was the dominant direction of travel. Accounts from 23rd August corroborate this, with ash reported in the north east in the straits of Sunda by ships such as the Princess Wihelmina (Macleod 1884), and heavy rains of pumice in the north in Lampong Bay on 26th August. The north east direction of travel may indicate that the summit of Danan (> 400 m) to the south, acted as a topographic barrier to PDC transport.

The massive PDC deposits of Unit D (Figures 5b; 5c; 7) emanate from the inferred caldera centre, with a dominant direction of travel towards the south west (Figure 8c). The change in PDC transport direction could indicate that the topographic barrier formed by Danan had been diminished by this stage, perhaps due to collapse associated with the emplacement of the lithic lag breccias comprising Unit C (Figures 4c; 5a; 5b).

The thick, structureless PDC deposits emplaced as part of Unit D may correspond to the paroxysmal explosions in the morning of 27th August 1883. At the top of Unit D, a lithic lag breccia is observed at locality D3S2/NP4 (Figure 5b), and at D2S2/U23 there are intensely fractured metre-scale glassy blocks (Figure 5c). These blocks are reminiscent of the large lava blocks found in phase 3 of 4 of the Late Bronze Age (Minoan) eruptive sequence in Santorini (Druitt and Francaviglia 1992; Sparks and Wilson 1990). By analogy, lava blocks originating from the volcanic island may have been entrained by PDCs. However, matrix glass analyses of the blocks, and smaller obsidian clasts, in Unit D of the 1883 stratigraphy, show that their chemistry is similar to the 1883 pyroclastic sequence, but extend to more evolved compositions (Figure 12). This chemistry is distinct from the range of 1883 lithic compositions noted by Mandeville et al. (1996b), which are predominantly basalt and basaltic andesite. The broadly consistent matrix glass chemistry of these block means it is likely that they are derived from the same source. Given the broad compositional similarities, they may be directly related to the magma that fed the 1883 eruption. In addition, the rounded, irregular “tear-drop” shapes of these blocks (Figure 5c) suggest ductile deformation during hot emplacement, making it likely that they erupted concurrently with the pyroclastic material. Given that the blocks are found in Unit D, at the top of the stratigraphic sequence (Figure 7), and the fact that they have not undergone fragmentation, one hypothesis for their formation is that they were small, stagnant, pockets of highly evolved melt in the shallow crust that were excavated and incorporated with the pyroclastic material during the final stages of caldera formation.

915 This section of the stratigraphy potentially corresponds to the largest explosion, and most
916 devastating tsunami, at 10 am on 27th August 1883.

917 No textural evidence for phreatomagmatic activity was found in Unit D. This is contrary to
918 what might be expected if the caldera collapse promoted significant magma-water
919 interaction. However, there are records of ash falling as "rounded accretions" in Java after the
920 main paroxysm (equated to Unit D; Figure 2), which may provide evidence for some magma
921 interacting with water during or after caldera collapse. However, the lack of fine-grained,
922 highly fragmented ash in Unit D is quite striking, particularly when compared with a "wet"
923 ignimbrite such as Oruanui (Allan et al., 2012), making it unlikely that water entered the vent
924 in significant amounts.

925 The deposits from the 1883 Krakatau eruption are consistent with those observed in many
926 caldera-forming eruptions, e.g., Bishop Tuff (Hildreth and Wilson, 2007), Crater Lake (Bacon,
927 1983; Kamata et al., 1993) and Santorini (Druitt et al., 2019). These eruptions commonly start
928 with a Plinian plume, with the single vent widening through time and PDCs contributing to an
929 increasing proportion of the erupted products. Caldera collapse then occurs when a critical
930 volume of magma has been removed from the plumbing system beneath. The tapping of
931 multiple melt batches has been documented for many crystal-poor, caldera-forming
932 eruptions, particularly in systems undergoing active extension, similar to Krakatau, e.g., the
933 Snake River Plain (Ellis et al., 2010; Ellis and Wolff, 2012) and the Taupo Volcanic Zone (Brown
934 et al., 1998; Charlier et al., 2003; Gravley et al., 2007; Wilson and Charlier, 2009; Bégué et al.,
935 2014). In these cases, melt was stored in laterally (rather than vertically) extensive systems,
936 with a consistent bulk chemistry between melt lenses (Cashman and Giordano 2014). Many
937 caldera-forming eruptions are preceded by some form of precursory eruption, however the
938 period of time between this and the climactic eruption is often poorly constrained (e.g., Allan
939 et al., 2012; Cashman and Giordano 2014; Druitt et al., 2019). The 1883 eruption of Krakatau

is unique in the sense that we know when this precursory activity began (Figure 2; 20th May 1883) from direct observations. This may be invaluable for monitoring volcanoes with a history of producing explosive, caldera-forming eruptions, because it highlights the potential for a large event to follow a relatively moderate explosive eruption, on a timescale of months. However, the identification of such events as precursory to an incipient larger eruption remains challenging. Although a precursory Plinian eruption might increase the risk of a larger eruption, one does not always follow on from the other. Top-down factors, such as the removal of mass from the volcano edifice (discussed in section 5.4), potentially have a role in triggering these devastating paroxysms. Therefore, it would also be useful to carefully monitor surface deformation and any significant losses of mass at Anak Krakatau, as well as other similar volcanic systems.

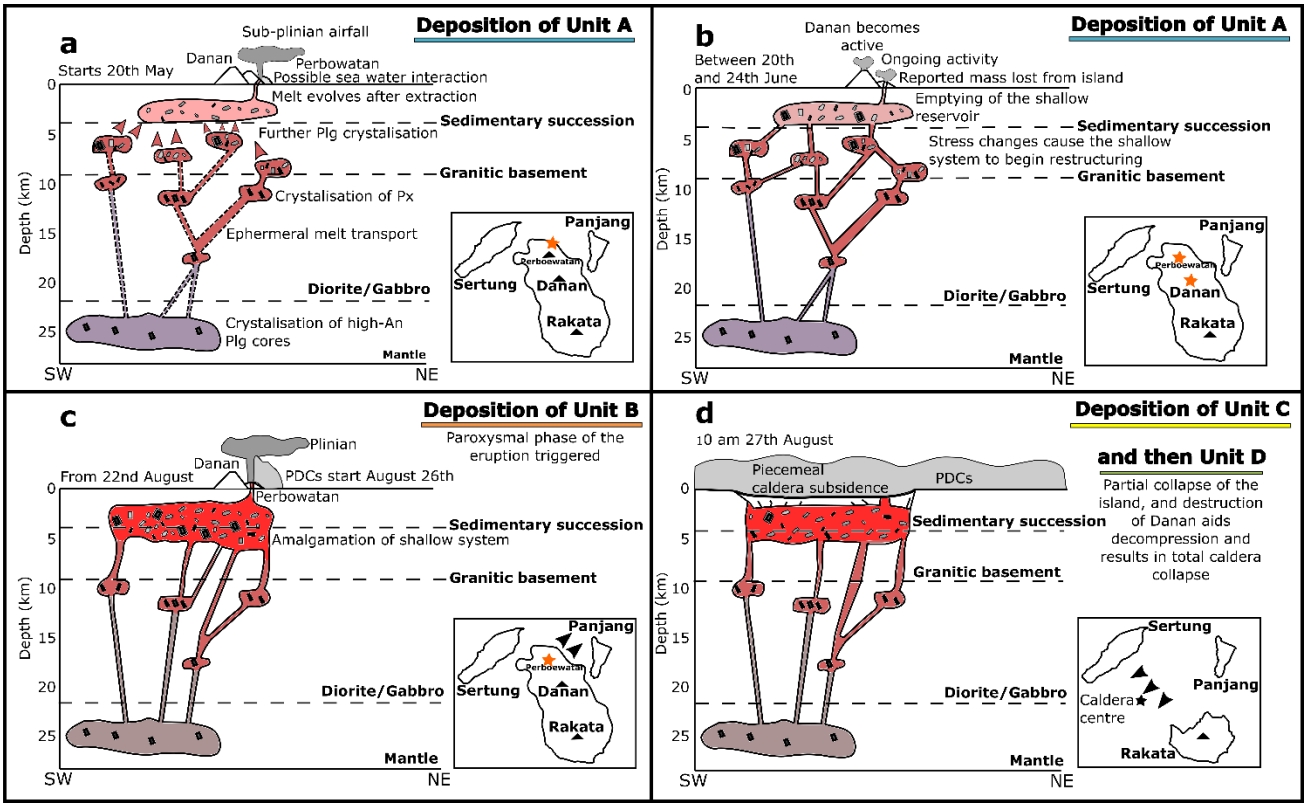

Figure 14: Series of schematic diagrams coupled with plan view maps illustrating one possible model for the magmatic and eruptive evolution of the 1883 eruption of Krakatau (lithological structure and crystallisation depths from Darhen et al., 2012). On maps orange stars indicate

an active edifice, and black arrows represent the dominant direction of PDCs. Dashed lines on schematic cross sections indicate ephemeral transport pathways of magma. Red arrows indicate melt extraction. Colours of melt represent melt composition: Purple for the least evolved, followed by brown, bright red, with pink representing the most silicic melt. Panel (a) shows the deposition of Unit A (Figure 7), with evidence for a more silicic reservoir derived from matrix glass analyses (Figure 12), and the observed eruption dynamics (Figure 2). Panel (b) shows observed changes to the eruption dynamics (Figure 2), and proposed system restructuring. Panel (c) shows the deposition of Unit B (Figure 7), and the start of the paroxysmal phases of the eruption, as determined by observations (Figure 2), as well as syn-eruptive mixing of chemically similar melt batches hypothesised as a result of varied and complex plagioclase textures and chemistry (Figure 10; 11), and only minor variations in matrix glass chemistry (Figure 12). Panel (d) shows the deposition of Unit C and Unit D in a piecemeal caldera collapse, as there are two lithic lag breccias (Figure 7), and a substantial change in PDC and dilute-PDC directionality (Figure 8).

6 Conclusions

This study presents field observations from new exposures of the 1883 eruptive deposits of Krakatau, revealed as a result of the removal of vegetation by the 2018 tsunami generated by flank collapse of Anak Krakatau. This has allowed for the stratigraphy of the eruption to be considerably better constrained (Figure 3; Figure 7). Examination of the geochemistry in the context of this refined eruptive stratigraphy does not support previous studies (e.g., Mandeville et al., 1996a) that have proposed that the eruption emanated from a chemically zoned magma reservoir. An updated model for the magmatic system is proposed, accounting for the chemical variations in context with the stratigraphic sequence.

The existence of a distinct, green, basal ashfall (Figure 4a) is consistent with written accounts of precursory activity in May (e.g., Symons et al., 1888; Figure 2), with the matrix glass chemistry indicating a shallow, more silicic melt-rich region was tapped during this preliminary eruptive phase (Figure 12). It is likely that restructuring of the magmatic system and syn-eruptive mixing of multiple chemically similar melt batches then occurred, to account for the chemical homogeneity in pyroclasts in Units B to D (Figure 12), and complex plagioclase phenocryst zoning profiles and textures (Figures 10 and 11). This restructuring may have occurred simply as a result of gradual emptying of the initial silicic reservoir, however the loss of mass reported from the summits of Perboewatan and/or Danan (Figure 1) may also have played a role. The stress changes and reservoir reconstruction may have contributed to the onset of the climactic phase of the eruption on 26th August.

There is a substantial change in the directionality of the PDCs throughout the climactic phase of the eruption (Figure 8), which coincides with the deposition of a lithic lag breccia occupying a distinct horizon within the stratigraphy (Figure 4c; 5a; 5b). The lithic lag breccia is thus attributed to partial collapse of the island, and the removal of the edifice Danan as a topographic barrier. The 1883 eruption culminated in total caldera collapse, which, together with the PDC production at this stage, was a potential cause of the largest tsunami at 10 am on 27th August. This final caldera collapse is recorded in the stratigraphy as a second lithic lag breccia (Figure 5b), and at one locality (U23/D2S2) glassy blocks up to 8 m in size are present (Figure 5c), which are reported within this sequence for the first time here. The matrix glass chemistry of these blocks (Figure 12) suggests that they are derived from the same melt as the 1883 pyroclastic material, and their shapes suggest that they underwent ductile deformation during hot emplacement.

The identification of at least two lag breccias may indicate piecemeal caldera formation, where the first stage of collapse is the driving force behind the most energetic and explosive, climactic part of the eruption. Precursory Plinian eruptions are therefore very useful phenomena to be

aware of for the future monitoring of volcanoes with a history of producing silicic caldera-forming eruptions. The 1883 eruption of Krakatau provides an example of an event where relatively moderate explosive eruptions may potentially have run-away effects culminating in cataclysmic caldera-collapse several months later.

7 Acknowledgements

With thanks to V. Smith, P. Gopon, J. Wade and E. Johnson for help using electron imaging facilities; O. Green and J. Wells for help with sample preparation; S. Day and S. Carey for useful discussions; A. Novellino for help on 2019 field campaign; and the British Geological Survey for the loan of historical samples. DRT and SLE publish with permission of the CEO, British Geological Survey (United Kingdom Research and Innovation). Lastly, thank you to S. Self, B. Andrews and one anonymous reviewer for their insightful feedback on the manuscript during the review process.

Funding: This work was supported by the Natural Environment Research Council (NERC). ALM-N acknowledges NERC Studentship NE/L202612/1; MC acknowledges NERC fellowship NE/N014286/1; MC, SW, SLE, and MA acknowledge a NERC urgency grant NE/T002026/1; DMP and TM acknowledge support from NERC COMET; MA acknowledges Program Riset Unggulan ITB 2020 grant.

8 Data availability

Datasets related to this article can be found at https://www.bgs.ac.uk/services/ngdc/accessions/index.html#item137445 , hosted at National Geological Data Centre by the British Geological Survey (Madden-Nadeau, 2020).

9 References

1029 Abdurrachman, M., Widiyantoro, S., Priadi, B. and Ismail, T. (2018). Geochemistry and
1030 Structure of Krakatoa Volcano in the Sunda Strait, Indonesia. Geosciences, 8(4), 111.

1031 Algemeen Dagblad (1883). 20th and 26th June, 17th and 27th August, 3rd, 5th and 11th
1032 September.

1033 Allan, A.S., Wilson, C.J., Millet, M.A. and Wysoczanski, R.J. (2012). The invisible hand:
1034 Tectonic triggering and modulation of a rhyolitic supereruption. Geology, 40(6), 563-566.

1035 Anderson, D.J. and Lindsley, D.H. (1988). Internally consistent solution models for Fe-Mg-Mn-
1036 T: Oxides. Am. Mineral, 66, 416-420.

1037 Andrews, B.J., Gardner, J.E. and Housh, T.B. (2008). Repeated recharge, assimilation, and
1038 hybridization in magmas erupted from El Chichón as recorded by plagioclase and amphibole
1039 phenocrysts. Journal of Volcanology and Geothermal Research, 175(4), 415-426.

1040 Andrews, B.J. and Manga, M. (2014). Thermal and rheological controls on the formation of
1041 mafic enclaves or banded pumice. Contributions to Mineralogy and Petrology, 167(1), 1-16.

1042 Ashdown, E. (1883). A Floating Lava Bed [Letter to the editor, reprinted from the London
1043 Times]. Nature, 28:532-533.

1044 Bacon, C.R. (1983). Eruptive history of Mount Mazama and Crater Lake caldera, Cascade
1045 Range, USA. Journal of Volcanology and Geothermal Research, 18(1-4), 57-115.

1046 Bacon, C. R. and Hirschmann, M. M. (1988). Mg/Mn partitioning as a test for equilibrium
1047 between coexisting Fe-Ti oxides. American Mineralogist, 73(1-2), 57-61.

1048 Bataviaasch Handelsblad (1883). 16th and 28th August, and 9th September.

1049 Bégué, F., Deering, C.D., Gravley, D.M., Kennedy, B.M., Chambefort, I., Gualda, G.A. and
1050 Bachmann, O. (2014). Extraction, storage and eruption of multiple isolated magma batches in the
1051 paired Mamaku and Ohakuri eruption, Taupo Volcanic Zone, New Zealand. Journal of
1052 Petrology, 55(8), 1653-1684.

1053 Blake, S., 1984. Volatile oversaturation during the evolution of silicic magma chambers as an
1054 eruption trigger. Journal of Geophysical Research: Solid Earth, 89(B10), 8237-8244.

1055 Blundy, J., Cashman, K.V., Rust, A. and Witham, F. (2010). A case for CO2-rich arc
1056 magmas. Earth and Planetary Science Letters, 290(3-4), 289-301.

1057 Branney, M. J. and Kokelaar, B. P. (2002). Pyroclastic density currents and the sedimentation
1058 of ignimbrites. Geological Society of London.

1059 Brown, R.J., Branney, M.J., Maher, C. and Dávila-Harris, P. (2010). Origin of accretionary lapilli
1060 within ground-hugging density currents: evidence from pyroclastic couplets on
1061 Tenerife. Bulletin, 122(1-2), 305-320.

1062 Brown, S.J.A., Wilson, C.J.N., Cole, J.W. and Wooden, J. (1998). The Whakamaru group
1063 ignimbrites, Taupo Volcanic Zone, New Zealand: evidence for reverse tapping of a zoned silicic
1064 magmatic system. Journal of Volcanology and Geothermal Research, 84(1-2), 1-37.

1065 Burgisser, A., Poussineau, S., Arbaret, L., Druitt, T.H., Giachetti, T. and Bourdier, J.L. (2010).
1066 Pre-explosive conduit conditions of the 1997 Vulcanian explosions at Soufrière Hills Volcano,
1067 Montserrat: I. Pressure and vesicularity distributions. Journal of Volcanology and Geothermal
1068 Research, 194(1-3), 27-41.

1069 Camus, G., Gourgaud, A. and Vincent, P. M. (1987). Petrologic evolution of Krakatau
1070 (Indonesia): implications for a future activity. Journal of Volcanology and Geothermal
1071 Research, 33(4), 299-316.

1072 Cashman, K. V. and Giordano, G. (2014). Calderas and magma reservoirs. Journal of
1073 Volcanology and Geothermal Research, 288, 28-45.

1074 Cassidy, M., Castro, J.M., Helo, C., Troll, V.R., Deegan, F.M., Muir, D., Neave, D.A. and
1075 Mueller, S.P. (2016). Volatile dilution during magma injections and implications for volcano
1076 explosivity. Geology, 44(12), 1027-1030.

1077 Cassidy, M., Edmonds, M., Watt, S.F.L., Palmer, M.R. and Gernon, T.M. (2015). Origin of
1078 basalts by hybridization in andesite-dominated arcs. Journal of Petrology, 56(2), 325-346.

1079 Cassidy, M., Manga, M., Cashman, K. and Bachmann, O. (2018). Controls on explosive-
1080 effusive volcanic eruption styles. Nature communications, 9(1), 1-16.

1081 Ceylon Observer (1883). The Volcanic Eruption in the Sunda Straits. 6 Sep.

1082 Charlier, B.L., Peate, D.W., Wilson, C.J., Lowenstern, J.B., Storey, M. and Brown, S.J., (2003).
1083 Crystallisation ages in coeval silicic magma bodies: 238U–230Th disequilibrium evidence from the
1084 Rotoiti and Earthquake Flat eruption deposits, Taupo Volcanic Zone, New Zealand. Earth and
1085 Planetary Science Letters, 206(3-4), 441-457.

1086 Cheng, L., Costa, F. and Carniel, R. (2017). Unraveling the presence of multiple plagioclase
1087 populations and identification of representative two-dimensional sections using a statistical and
1088 numerical approach. American Mineralogist, 102, 1894–1905

1089 Christopher, T.E., Blundy, J., Cashman, K., Cole, P., Edmonds, M., Smith, P.J., Sparks, R.S.J.,
1090 and Stinton, A. (2015). Crustal-scale degassing due to magma system destabilization and magma-
1091 gas decoupling at Soufrière Hills Volcano, Montserrat." Geochemistry, Geophysics,
1092 Geosystems, 16(9), 2797-2811.

1093 Cioni, R., Gurioli, L., Sbrana, A. and Vougioukalakis, G. (2000). Precursory phenomena and
1094 destructive events related to the Late Bronze Age Minoan (Thera, Greece) and AD 79 (Vesuvius,
1095 Italy) Plinian eruptions; inferences from the stratigraphy in the archaeological areas. Geological
1096 Society, London, Special Publications, 171(1), 123-141.

1097 Costa, F., Shea, T. and Ubide, T. (2020). Diffusion chronometry and the timescales of magmatic
1098 processes. Nature Reviews Earth & Environment, 1(4), 201-214.

1099 Dahren, B., Troll, V. R., Andersson, U. B., Chadwick, J. P., Gardner, M. F., Jaxybulatov, K. and
1100 Koulakov, I. (2012). Magma plumbing beneath Anak Krakatau volcano, Indonesia: evidence for
1101 multiple magma storage regions. Contributions to Mineralogy and Petrology, 163(4), 631-651.

1102 Deplus, C., Bonvalot, S., Dahrin, D., Diament, M., Harjono, H. and Dubois, J. (1995). Inner
1103 structure of the Krakatau volcanic complex (Indonesia) from gravity and bathymetry data. Journal
1104 of Volcanology and Geothermal Research, 64(1-2), 23-52.

1105 Druitt, T. H., Costa, F., Deloule, E., Dungan, M. and Scaillet, B. (2012). Decadal to monthly
1106 timescales of magma transfer and reservoir growth at a caldera volcano. Nature, 482(7383), 77-
1107 80.

1108 Druitt, T. H. and Francaviglia, V. (1992). Caldera formation on Santorini and the physiography
1109 of the islands in the late Bronze Age. Bulletin of Volcanology, 54(6), 484-493.

Druitt, T. H. and Sparks, R. S. J. (1982). A proximal ignimbrite breccia facies on Santorini, Greece. Journal of Volcanology and Geothermal Research, 13(1-2), 147-171.

Druitt, T.H., Pyle, D.M. and Mather, T.A. (2019). Santorini volcano and its plumbing system. Elements 15, 177-184.

Edmonds, M. (2008). New geochemical insights into volcanic degassing. Philosophical Transactions of the Royal Society A: Mathematical, Physical and Engineering Sciences, 366(1885), 4559-4579.

Ellis, B.S., Barry, T., Branney, M.J., Wolff, J.A., Bindeman, I., Wilson, R. and Bonnichsen, B., (2010). Petrologic constraints on the development of a large-volume, high temperature, silicic magma system: The Twin Falls eruptive centre, central Snake River Plain. Lithos, 120(3-4), 475-489.

Ellis, B.S. and Wolff, J.A., (2012). Complex storage of rhyolite in the central Snake River Plain. Journal of Volcanology and Geothermal Research, 211, 1-11.

Forni, F., Degruyter, W., Bachmann, O., De Astis, G. and Mollo, S. (2018). Long-term magmatic evolution reveals the beginning of a new caldera cycle at Campi Flegrei. Science advances, 4(11).

Francis, P. and Self, S. (1983). The eruption of Krakatau. Scientific American, 249(5), 172-187.

Furneaux (1964). Krakatoa. New Jersey, Prentice Hall.

Gardner, M.F., Troll, V.R., Gamble, J.A., Gertisser, R., Hart, G.L., Ellam, R.M., Harris, C. and Wolff, J.A. (2012). Crustal differentiation processes at Krakatau volcano, Indonesia. Journal of Petrology, 54(1), pp.149-182.

Geschwind, C. H. and Rutherford, M. J. (1992). Cummingtonite and the evolution of the Mount St. Helens (Washington) magma system: an experimental study. Geology, 20(11), 1011-1014.

Ghiorso, M. S. and Evans, B. W. (2008). Thermodynamics of rhombohedral oxide solid solutions and a revision of the Fe-Ti two-oxide geothermometer and oxygen-barometer. American Journal of Science, 308(9), 957-1039.

Ginibre, C., Wörner, G. and Kronz, A. (2002). Minor-and trace-element zoning in plagioclase: implications for magma chamber processes at Parinacota volcano, northern Chile. Contributions to Mineralogy and Petrology, 143(3), 300-315.

Gorshkov, G. S. (1959). Gigantic eruption of the volcano Bezymianny. Bulletin Volcanologique, *20*(1), 77-109.

Gottsmann, J. and Marti, J. (eds) Caldera Volcanism: Analysis, Modelling and Response (Dev. Volcanol. 10, Elsevier, 2008)

Grainger (1883). Algemeen Dagblad, 23rd May.

Gravley, D.M., Wilson, C.J.N., Leonard, G.S. and Cole, J.W., (2007). Double trouble: Paired ignimbrite eruptions and collateral subsidence in the Taupo Volcanic Zone, New Zealand. Geological Society of America Bulletin, 119(1-2),18-30.

Grilli, S. T., Tappin, D. R., Carey, S., Watt, S. F., Ward, S. N., Grilli, A. R. and Muin, M. (2019). Modelling of the tsunami from the December 22, 2018 lateral collapse of Anak Krakatau volcano in the Sunda Straits, Indonesia. Scientific reports, 9(1), 1-13

Gualda, G.A., Ghiorso, M.S., Lemons, R.V. and Carley, T.L. (2012). Rhyolite-MELTS: a modified calibration of MELTS optimized for silica-rich, fluid-bearing magmatic systems. Journal of Petrology, 53(5), 875-890.

Hall, R. (2012). Late Jurassic–Cenozoic reconstructions of the Indonesian region and the Indian Ocean. Tectonophysics, 570, 1-41.

Hall, R. and Spakman, W. (2002). Subducted slabs beneath the eastern Indonesia–Tonga region: insights from tomography. Earth and Planetary Science Letters, 201(2), 321-336.

Harjono, H., Diament, M., Nouaili, L. and Dubois, J. (1989). Detection of magma bodies beneath Krakatau volcano (Indonesia) from anomalous shear waves. Journal of volcanology and geothermal research, 39(4), 335-348.

Hesse, E.D. (1690). Ost Indiamische Reise-Beschreibung oder Diariu, Leipzig.

Hesse, E.D. (1694). Drie Seer Aanmerkelyke Reysen na en door Verlerley Gewesten in Oost-Indien; gedaan door Christophorus Frikius, Chirugyn, Elias Hesse, Berghschryver, Christophorus

1162 Schweitzer, Boekhouder; Yeder Bysonder; van ‘t Jaer 1675 tot 1686. Translated from German to
1163 Dutch by Simon de Vries. Utrecht.

1164 Hildreth, W. and Wilson, C. J. (2007). Compositional zoning of the Bishop Tuff. Journal of
1165 Petrology, 48(5), 951-999.

1166 Javasche Courant (1883). 20th July.

1167 Jaxybulatov, K., Koulakov, I., Ibs-von Seht, M., Klinge, K., Reichert, C., Dahren, B. and Troll,
1168 V.R. (2011). Evidence for high fluid/melt content beneath Krakatau volcano (Indonesia) from local
1169 earthquake tomography. Journal of Volcanology and Geothermal Research, 206(3-4), 96-105.

1170 Joly, J. (1885) Notes on the microscopical character of the volcanic ash from Krakatoa.
1171 Proceedings of the Royal Dublin Society, 4, 291-299.

1172 Kamata, H., Suzuki-Kamata, K. and Bacon, C.R. (1993). Deformation of the Wineglass Welded
1173 Tuff and the timing of caldera collapse at Crater Lake, Oregon. Journal of Volcanology and
1174 Geothermal Research, 56(3), pp.253-265.

1175 Knesel, K.M., Davidson, J.P. and Duffield, W.A. (1999). Evolution of silicic magma through
1176 assimilation and subsequent recharge: evidence from Sr isotopes in sanidine phenocrysts, Taylor
1177 Creek Rhyolite, NM. Journal of Petrology, 40(5), 773-786.

1178 LaTourrette, T. and Wasserburg, G.J. (1998). Mg diffusion in anorthite: implications for the
1179 formation of early solar system planetesimals. Earth and Planetary Science Letters, 158(3-4), 91-
1180 108.

1181 Latter, J.H. (1981). Tsunamis of Volcanic Origin: Summary of Causes, with Particular
1182 Reference to Krakatau, 1883. Bulletin Volcanologique, 44:467-490.

1183 Le Bas, M.J., Le Maitre, R. W., Streckeisen, A., Zanettin, B. and IUGS Subcommission on the
1184 Systematics of Igneous Rocks. (1986). A chemical classification of volcanic rocks based on the
1185 total alkali-silica diagram. Journal of petrology, 27(3), 745-750.

1186 Lindemann, T.H. (1884). Report from H.B.M Consol at Batavia, inclosing extracts relating to
1187 the volcanic outburst in the Sunda Strait, from the logbook of the steamship Governor-General
1188 Loudon. Proceedings of the Royal Society of London, 36, 199-203.

Lindsley, D. H. and Frost, B. R. (1992). Equilibria among Fe-Ti oxides, pyroxenes, olivine, and quartz: Part I. Theory. American Mineralogist, 77(9-10), 987-1003.

Lunt, P., Burgon, G., and Baky, A. (2009). The Pemali Formation of Central Java and equivalents: Indicators of sedimentation on an active plate margin. Journal of Asian Earth Sciences, 34(1), 100-113.

MacKenzie (1883). Java Bode, 30 May.

Macleod (1884). De Uitbarsting van de Krakatau. Tijdschift van het Koninklijk Nederlandsch Aardrijk-skundig Genootschap, 2, 1: 184-191

[dataset] Madden-Nadeau, A.L. (2020): Geochemical and petrological data pertaining to the eruptive deposits of 1883 caldera-forming eruption of Krakatau. British Geological Survey. (Dataset). https://doi.org/10.5285/ad2a4fa0-7b66-4ec5-a5cf-d78944716ec4.

Mandeville, C.W., Carey, S. and Sigurdsson, H. (1996a). Magma mixing, fractional crystallization and volatile degassing during the 1883 eruption of Krakatau volcano, Indonesia. Journal of Volcanology and Geothermal Research, 74(3-4), 243-274.

Mandeville, C. W., Carey, S. and Sigurdsson, H. (1996b). Sedimentology of the Krakatau 1883 submarine pyroclastic deposits. Bulletin of Volcanology, 57(7), 512-529.

Metzger, E. (1884). Gleanings from Reports Concerning the Eruption of Krakatoa. Nature, 29:240-244.

Mollo, S., Putirka, K., Iezzi, G., Del Gaudio, P. and Scarlato, P. (2011). Plagioclase–melt (dis) equilibrium due to cooling dynamics: implications for thermometry, barometry and hygrometry. Lithos, 125(1-2), 221-235.

Nelson, S.T. and Montana, A. (1992). Sieve-textured plagioclase in volcanic rocks produced by rapid decompression. American Mineralogist, 77(11-12), 1242-1249.

Newhall, C. G. and Dzurisin, D. (1988) Historical Unrest at Large Calderas of the World Vols 1 and 2, Bull. US Geol. Surv. 1855, USGS.

Newman, S. and Lowenstern, J.B. (2002). VolatileCalc: a silicate melt–H_2O–CO_2 solution model written in Visual Basic for excel. Computers and Geosciences, 28, 597-604.

Ninkovich, D. (1976). Late Cenozoic clockwise rotation of Sumatra. Earth and Planetary Science Letters, 29(2), 269-275.

Ninkovich, D. (1979). Distribution, age and chemical composition of tephra layers in deep-sea sediments off western Indonesia. Journal of Volcanology and Geothermal Research, 5(1-2), 67-86.

Nishimura, S., Harjono, H. and Suparka, S. (1992). The Krakatau Islands: the geotectonic setting. GeoJournal, 28(2), 87-98.

Novellino, A., Engwell, S.L., Grebby, S., Day, S., Cassidy, M., Madden-Nadeau, A.L., Watt, S., Pyle, D., Abdurrachman, M., Edo Marshal Nurshal, M. and Tappin, D.R. (2020). Mapping recent shoreline changes spanning the lateral collapse of Anak Krakatau Volcano, Indonesia. Applied Sciences, 10(2), 536.

Oba, N., Tomita, K., Yamamoto, M., Istidjab, M. and Badruddin, M. (1982). Geochemical study of lava flows, ejecta and pyroclastic flow from the Krakatau Group, Indonesia. Kagoshima Daigaku Rigakubu kiyō. Chigaku seibutsugaku, 15, 41-76.

Probst, L.C., Sheldrake, T.E., Gander, M.J., Wallace, G., Simpson, G. and Caricchi, L. (2018). A cross correlation method for chemical profiles in minerals, with an application to zircons of the Kilgore Tuff (USA*).* Contributions to Mineralogy and Petrology, 173(3), 23.

Rossi, S., Petrelli, M., Morgavi, D., Vetere, F.P., Almeev, R.R., Astbury, R.L. and Perugini, D. (2019). Role of magma mixing in the pre-eruptive dynamics of the Aeolian Islands volcanoes (Southern Tyrrhenian Sea, Italy). Lithos, 324, 165-179.

Ruprecht, P., Bergantz, G.W., Cooper, K.M. and Hildreth, W. (2012). The crustal magma storage system of Volcán Quizapu, Chile, and the effects of magma mixing on magma diversity. Journal of Petrology, 53(4), 801-840.

Rutherford, M. J. and Devine, J. D. (1988). The May 18, 1980, eruption of Mount St. Helens: 3. Stability and chemistry of amphibole in the magma chamber. Journal of Geophysical Research: Solid Earth, *93*(B10), 11949-11959.

1241 Schlüter, H.U., Gaedicke, C., Roeser, H.A., Schreckenberger, B., Meyer, H., Reichert, C.,
1242 Djajadihardja, Y. and Prexl, A. (2002). Tectonic features of the southern Sumatra-western Java
1243 forearc of Indonesia. Tectonics, 21(5), pp.11-1.

1244 Schwandt, C.S., Cygan, R.T. and Westrich, H.R. (1998). Magnesium self-diffusion in
1245 orthoenstatite. Contributions to Mineralogy and Petrology, 130(3-4), 390-396.

1246 Self, S. (1992). Krakatau revisited: the course of events and interpretation of the 1883
1247 eruption. GeoJournal, 28(2), 109-121.

1248 Self, S. and Rampino, M. R. (1981). The 1883 eruption of Krakatau. Nature, 294(5843), 699-
1249 704.

1250 Self, S. and Wohletz, K. H. (1983). A new look at initiation and timing of the Krakatau 1883
1251 eruption sequence. Eos, 64, 872.

1252 Shields, J. K., Mader, H. M., Caricchi, L., Tuffen, H., Mueller, S., Pistone, M. and Baumgartner,
1253 L. (2016). Unravelling textural heterogeneity in obsidian: Shear-induced outgassing in the Rocche
1254 Rosse flow. Journal of Volcanology and Geothermal Research, 310, 137-158.

1255 Sigurdsson, H., Cashdollar, S. and Sparks, S.R.J. (1982). The eruption of Vesuvius in A.D. 79
1256 A.D.: reconstruction from historical and volcanological evidence. American Journal of Archaeology
1257 86, 39-51.

1258 Simkin, T. and Fiske, R.S. (1983) Krakatau 1883: the volcanic eruption and its effects.
1259 Smithsonian Institution Press, Washington D.C., 464 pp.

1260 Sparks, R.S.J., Sigurdsson, H. and Wilson, L. (1977). Magma mixing: a mechanism for
1261 triggering acid explosive eruptions. Nature, 267(5609), 315-318.

1262 Sparks, R.S.J. and Wilson, C. J. N. (1990). The Minoan deposits: a review of their
1263 characteristics and interpretation. Thera and the Aegean world III, *2*, 89-99.

1264 Stehn, C. E. (1929). The geology and volcanism of the Krakatau group. Fourth Pacific Science
1265 Congress, 1-54.

1266 Sturdy, E.W. (1884). The volcanic eruption of Krakatau. Atlantic Monthly, 54, 385-391.

Sulzer (1883). Java Bode, 30th May.

Susilohadi, S., Gaedicke, C. and Djajadihardja, Y. (2009). Structures and sedimentary deposition in the Sunda Strait, Indonesia. Tectonophysics, *467*(1-4), 55-71.

Symons, G.J., Judd, J.W., Strachey, S.R., Wharton, W.J.L., Evans, F.J., Russell, F.A.R., Archibald, D. and Whipple, G.M. (1888). The eruption of Krakatoa and subsequent phenomena (p. 494). Trübner & Company.

Tagliche Rundchau (1883). Berlin, 255-256.

Tarasewicz, J., White, R.S., Woods, A.W., Brandsdóttir, B. and Gudmundsson, M.T. (2012). Magma mobilization by downward-propagating decompression of the Eyjafjallajökull volcanic plumbing system. Geophysical Research Letters, 39(19).

Tennison-Woods, J.E. (1884). The Earthquake in the Straits of Sunda. Sydney Morning Herald, 16-18 Jan.

Times of London (1883). 3 July:10, column f, and 8 October.

Tramontano, S., Gualda, G.A. and Ghiorso, M.S. (2017). Internal triggering of volcanic eruptions: Tracking overpressure regimes for giant magma bodies. Earth and Planetary Science Letters, 472, 142-151.

Turner, S. and Foden, J. (2001). U, Th and Ra disequilibria, Sr, Nd and Pb isotope and trace element variations in Sunda arc lavas: predominance of a subducted sediment component. Contributions to Mineralogy and Petrology, 142(1), 43-57.

Van Heerdt, P.T. (1884?) Report of Captain Visman of the Prinses Wilhelmina. Letter to Symons, G.J. at the Royal Society, London.

Verbeek, R.D.M. (1884). The Krakatoa Eruption 1. Nature, 30,10–15.

Verbeek, R.D.M. (1885). Krakatau. Batavia.

Viccaro, M., Giacomoni, P.P., Ferlito, C. and Cristofolini, R. (2010). Dynamics of magma supply at Mt. Etna volcano (Southern Italy) as revealed by textural and compositional features of plagioclase phenocrysts. Lithos, 116(1-2), 77-91.

Vogel, J.W. (1690). Journal einer Reise aus Holland nach Ost-In-dien. Frankfurt and Leipzig.

Walker (1884). Extracts from log of The Actea (May 20, 1883). Nature, 30.

Waters, L.E. and Lange, R.A. (2015). An updated calibration of the plagioclase-liquid hygrometer-thermometer applicable to basalts through rhyolites. American Mineralogist, 100(10), 2172-2184.

Watt, S.F.L. (2019). The evolution of volcanic systems following sector collapse. Journal of Volcanology and Geothermal Research, 384, 280-303.

Williams, R., Branney, M. J. and Barry, T. L. (2014). Temporal and spatial evolution of a waxing then waning catastrophic density current revealed by chemical mapping. Geology, 42(2), 107-110.

Wilson, C.J.N. and Charlier, B.L.A. (2009). Rapid rates of magma generation at contemporaneous magma systems, Taupo Volcano, New Zealand: insights from U–Th model-age spectra in zircons. Journal of Petrology, 50(5), 875-907.